Electronic Supplementary Material (ESI)

Anion-π recognition between $[M(CN)_6]^{3-}$ complexes and $HAT(CN)_6$: structural matching and electronic charge density modification

Jędrzej Kobylarczyk, Dawid Pinkowicz, Monika Srebro-Hooper, James Hooper, and Robert Podgajny*

[a]Faculty of Chemistry, Jagiellonian University in Krakow, Ingardena 3, 30-060 Krakow, Poland. E-mail: robert.podgajny@uj.edu.pl

Contents of Electronic Supplementary Material

I. Experimental part

Synthesis procedures and preliminary characteristic

$HAT(CN)_6$. Hexaketocyclohexane octahydrate (2.0 g , 6.4 mmol) and diaminomaleonitrile (5.2 g, 48 mmol) were dissolved in 250 ml of glacial AcOH. The mixture was heated in reflux for 2 h. Resulting dark brown-black mixture was filtered and washed with hot glacial AcOH (3 x 40 ml). Obtained black solid was suspended into 35 % HNO_3 (40 ml) and was heated to 100°C for 3 hours. Crude product was obtained by mixture cooled to room temperature, poured into small portion of ice and filtered off. Purification of $HAT(CN)_6$ was performed by continuous extraction in Soxhlet apparatus (100 mL MeCN, 72 h, high reflux). Acetonitrile was removed by vacuum evaporation to give orange solid. Yield: 1.88 g, 77 %. IR (cm^{-1}): 2256 *ν*(C≡N), 2241 *ν*(C≡N), 1713, 1622, 1528, 1467, 1458, 1400, 1342, 1317, 1249, 1237, 1200, 1146, 1084, 1052, 920, 809, 749, 706. ^{13}C NMR (300 MHz, CD_3CN) δ (ppm): 112.9 , 135.4, 142.1

$(PPh_4)_3[Fe(CN)_6]\cdot HAT(CN)_6$ (1). Acetonitrile solutions of $(PPh_4)_3[Fe(CN)_6]\cdot 6H_2O$ (0.2452 g, 0.18 mmol, 8 ml) and $HAT(CN)_6$ (0.0383 g, 0.1 mmol, 12 ml) were mixed to give a dark-green solution immediately. The solution was stirred for 30 min. The crystals of **1** suitable for crystallographic measurements were obtained by diffusion of diethyl ether vapour into this mixture. The green needle like crystals appeared after 1 day, then they were filtrated and washed with small amount of cold acetonitrile (4ml, -10°C) and dried in air. Yield: 132.4 mg, 82 %. Elemental analysis. Calcd for $C_{96}H_{60}N_{18}P_3Fe$: C, 71.4; H, 3.7; N, 15.6. Found: C, 71.1; H, 3.6; N, 15.6. IR ($(PPh_4)_3[Fe(CN)_6]$, a index; HAT-CN_6, b index) (cm^{-1}): 3066 *ν*(C-H)[a], 3065 *ν*(C-H)[a], 2244 *ν*(C≡N)[b], 2236 *ν*(C≡N)[b], 2115 *ν*(C≡N)[a], 2110 *ν*(C≡N)[a], 2098 *ν*(C≡N)[a], 1588[a], 1486[a], 1467[b] , 1442[a], 1437[a], 1342[b], 1317[a], 1249[b], 1237[b], 1190[a], 1151[b], 1113[a], 998[a], 854[a], 766[a], 758[a], 725[a], 699[a], 692[a].

$(PPh_4)_3[Co(CN)_6]\cdot HAT(CN)_6$ (2). Acetonitrile solutions of $(PPh_4)_3[Co(CN)_6]\cdot 7H_2O$ (0.2464 g, 0.18 mmol, 8 ml) and $HAT(CN)_6$ (0.0383 g, 0.1 mmol, 12 ml) were mixed to give a yellow solution immediately. The solution was stirred for 30 min. The crystals of **1** suitable for crystallographic measurements were obtained by diffusion of diethyl ether vapour into this mixture. The yellow needle like crystals appeared after 1 day, then they were filtrated and washed with small amount of cold acetonitrile (4ml, -10°C) and dried in air. Yield: 143.5 mg, 89 %. Elemental analysis. Calcd for $C_{96}H_{60}N_{18}P_3Co$: C, 71.3; H, 3.7; N, 15.6. Found: C, 71.0; H, 3.7; N, 15.5. . IR ($(PPh_4)_3[Co(CN)_6]$, a index; HAT-CN_6, b index) (cm^{-1}): 3086 *ν*(C-H)[a], 3065 *ν*(C-H)[a], 3017 *ν*(C-H)[a], 2244 *ν*(C≡N)[b], 2236 *ν*(C≡N)[b], 2132 *ν*(C≡N)[a], 2120 *ν*(C≡N)[a], 2108 *ν*(C≡N)[a], 1589[a], 1486[a], 1467[b], 1446[a], 1437[a], 1342[b], 1316[a], 1250[b], 1237[b], 1220[b], 1190[a], 1151[b], 1113[a], 998[a], 854[a], 767[a], 758[a], 725[a], 699[a], 691[a].

$(AsPh_4)_3[Fe(CN)_6]\cdot HAT(CN)_6\cdot 2CH_3CN\cdot H_2O$ (3). Acetonitrile solutions of $(AsPh_4)_3[Fe(CN)_6]\cdot 3H_2O$ (0.2724 g, 0.19 mmol 8 ml) and $HAT(CN)_6$ (0.0383 g, 0.1 mmol, 12 ml) were mixed to give a dark-green solution immediately. The solution was stirred for 30 min. The crystals of **3** suitable for crystallographic measurements were obtained by diffusion of diethyl ether vapour into this mixture. The green needle like crystals appeared after 1 day, then they were filtrated and washed with small amount of cold acetonitrile (4ml, -10°C). The composition of **3** was establish from crystal structure solution and refinement. While removed from solution exposed to ambient atmosphere, the crystals of **3** lose MeCN molecules and cracks visibly to produce the residue of the formula $(AsPh_4)_3[Fe(CN)_6]\cdot HAT(CN)_6\cdot 2H_2O$ (**3des**) deduced from elemental analysis. Yield: 110.3 mg, 60 %. Elemental analysis. Calcd. for $C_{96}H_{64}N_{18}As_3O_2Fe$ for $(AsPh_4)_3[Fe(CN)_6]HAT(CN)_6\cdot 2H_2O$: C, 64.7; H, 3.6; N, 14.2. Found: C, 64.9; H, 3.5; N, 14.2. TGA. The found weight loss of 2.2% in range 25-170 °C corresponds to the loss of 2 H_2O

molecules per formula unit (2.02%). IR ($(AsPh_4)_3[Fe(CN)_6]$, a index; $HAT(CN)_6$, b index) (cm^{-1}): 3082 *ν*(C-H)[a], 3061 *ν*(C-H)[a], 3022 *ν*(C-H)[a], 2247 *ν*(C≡N)[b], 2161 *ν*(C≡N)[a], 2101 *ν*(C≡N)[a], 2098 *ν*(C≡N)[a], 1656[a], 1580[a], 1484[a], 1466[b], 1442[a], 1342[b], 1314[a], 1247[b], 1235[b], 1221[b], 1187[a], 1151[b], 1083[a,b], 1051[b], 1024[a], 998[a], 986[a], 924[a,b], 851[a], 746[a,b], 690[a].

$(AsPh_4)_3[Co(CN)_6]\cdot HAT(CN)_6\cdot 2CH_3CN\cdot H_2O$ (4). Acetonitrile solutions of $(AsPh_4)_3[Co(CN)_6]\cdot 5H_2O$ (0.2732 g, 0.19 mmol 8 ml) and $HAT(CN)_6$ (0.0383 g, 0.1 mmol, 12 ml) were mixed to give a yellow solution immediately. The solution was stirred for 30 min. The crystals of **4** suitable for crystallographic measurements were obtained by diffusion of diethyl ether vapour into this mixture. The yellow needle like crystals appeared after 1 day, then they were filtrated and washed with small amount of cold acetonitrile (4ml, -10°C). The composition of **4** was establish from crystal structure solution and refinement. While removed from solution exposed to ambient atmosphere, the crystals of **4** lose MeCN molecules and crack visibly to produce the residue of the formula $(AsPh_4)_3[Fe(CN)_6]HAT(CN)_6\cdot 2H_2O$ (**4des**) deduced from elemental analysis. Yield: 116.4 mg, 62 %. Elemental analysis. Calcd for $C_{96}H_{64}N_{18}As_3O_2Co$ for $(AsPh_4)_3[Co(CN)_6]HAT(CN)_6\cdot 2H_2O$: C, 64.7.; H, 3.6; N, 14.2. Found: C, 64.6; H, 3.9; N, 14.1. The found weight loss of 1.9 % in range 25-240 °C corresponds to the loss of 2 H_2O molecules per formula unit (2.02%). IR ($(AsPh_4)_3[Co(CN)_6]$, a index; $HAT(CN)_6$ b index) (cm^{-1}): 3085 *ν*(C-H)[a], 3060 *ν*(C-H)[a], 3022 *ν*(C-H)[a], 2247 *ν*(C≡N)[b], 2243 *ν*(C≡N)[b], 2163 *ν*(C≡N)[a], 2131 *ν*(C≡N)[a], 2111 *ν*(C≡N)[a], 2108 *ν*(C≡N)[a], 1658[a], 1581[a], 1484[a], 1466[b], 1442[a], 1342[b], 1313[a], 1235[b], 1220[b], 1187[a], 1151[b], 1083[a,b], 1024[a], 998[a], 986[a], 924[a,b], 851[a], 746[a,b], 690[a].

II. Structural part

Table S1. Crystal data and structure refinement for **1** and **2**

Compound	**1**	**2**
empirical formula	$C_{96}H_{60}FeN_{18}P_3$	$C_{96}H_{60}CoN_{18}P_3$
formula weight	1614.38	1617.46
crystal system	trigonal	trigonal
space group	R3c	R3c
unit cell dimensions (Å, deg)	a = 27.6091(8) b = 27.6091(8) c = 18.7133(7) α = 90 β = 90 γ = 120	a = 27.5965(6) b = 27.5965(6) c = 18.6928(5) α = 90 β = 90 γ = 120
volume ($Å^3$)	12353.4(9)	12328.6(6)
Z	6	6
density, calcd ($mg \cdot m^{-3}$)	1.302	1.307
temp (K)	120.1	120
absorption coefficient (mm^{-1})	0.302	0.328
F(000)	4998.0	5004.0
wavelength (Å)	0.71073	0.71073
crystal size (mm^3)	0.4 × 0.1 × 0.08	0.65 × 0.14 × 0.12
2θ range for data collection (deg)	6.268 - 50.726	6.272 to 50.298
index ranges	-33 ≤ h ≤ 33 -32 ≤ k ≤ 33 -11 ≤ l ≤ 22	-31 ≤ h ≤ 32 -32 ≤ k ≤ 28 -22 ≤ l ≤ 22
reflections collected	16997	49834
independent reflections	3369 [R_{int} = 0.0421, R_{sigma} = 0.0339]	4871 [R_{int} = 0.0735, R_{sigma} = 0.0383]
completeness of θ (%)	100	100
max and min transmission	0.745 and 0.680	0.745 and 0.682
refinement method	Least Squares	Least Squares
data/restraints/parameters	3369/1/357	4871/1/356
goodness-of-fit on F^2	1.055	1.042
final R indices [I > 2σ(I)]	R_1 = 0.0300 wR_2 = 0.0672	R_1 = 0.0321 wR_2 = 0.0631
R indices (all data)	R_1 = 0.0348 wR_2 =0.0693	R_1 = 0.0412 wR_2 = 0.0660
extinction coefficient	0.00027(5)	none
largest diff. peak and hole ($e \cdot Å^{-3}$)	0.2700 and -0.3600	0.2500 and -0.2800

Table S2. Crystal data and structure refinement for **3** and **4**

Compound	**3**	**4**
empirical formula	$C_{100}H_{66}As_3FeN_{20}O$	$C_{100}H_{66}As_3CoN_{20}O$
formula weight	1844.33	1847.41
crystal system	monoclinic	monoclinic
space group	Cc	Cc
unit cell dimensions (Å, deg)	a = 20.9359(4) b = 27.5973(6) c = 17.7530(6) α = 90 β = 122.3080(10) γ = 90	a = 20.9033(7) b = 27.5801(11) c = 17.7843(10) α = 90 β = 122.388(2) γ = 90
volume ($Å^3$)	8669.3(4)	8658.0(7)
Z	4	4
density, calcd ($mg·m^{-3}$)	1.413	1.417
temp (K)	120	120
absorption coefficient (mm^{-1})	1.373	1.399
F(000)	3.756	3760.0
wavelength (Å)	0.71073	0.71073
crystal size (mm^3)	0.7 × 0.15 × 0.13	0.43 × 0.15 × 0.11
2θ range for data collection (deg)	5.904 to 52.476	5.908 to 55.828
index ranges	-25 ≤ h ≤ 26 -28 ≤ k ≤ 34 -22 ≤ l ≤ 22	-27 ≤ h ≤ 27 -36 ≤ k ≤ 24 -23 ≤ l ≤ 23
reflections collected	40105	49511
independent reflections	16750 [R_{int} = 0.0694, R_{sigma} = 0.0901]	19789 [R_{int} = 0.0524, R_{sigma} = 0.0665]
completeness of θ (%)	99	98
max and min transmission	0.745 and 0.624	0.746 and 0.593
refinement method	Least Squares	Least Squares
data/restraints/parameters	16750/2/1129	19789/2/1130
goodness-of-fit on F^2	1.021	1.018
final R indices [I > 2σ(I)]	R_1 = 0.0479 wR_2 = 0.0794	R_1 = 0.0376, wR_2 = 0.0658
R indices (all data)	R_1 = 0.0702, wR_2 = 0.0864	R_1 = 0.0503, wR_2 = 0.0697
extinction coefficient	none	none
largest diff. peak and hole ($e·Å^{-3}$)	0.5800 and – 0.4300	0.4300 and-0.4400

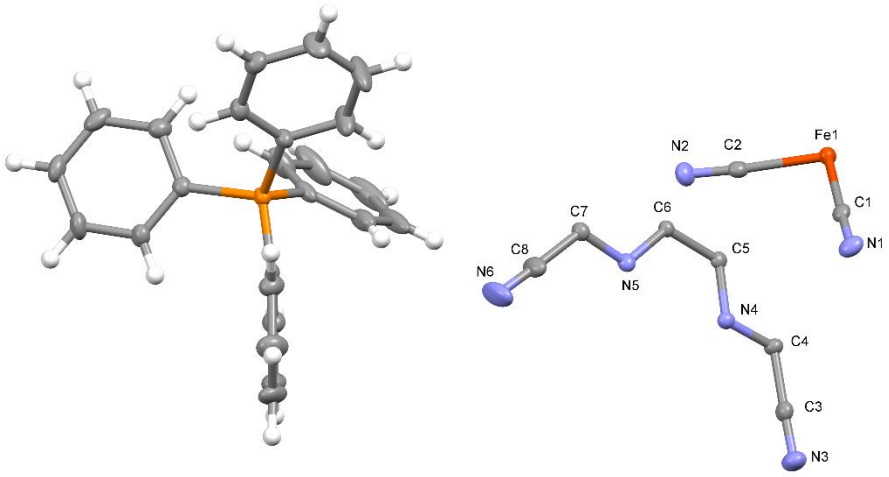

Figure S1. Asymmetric unit of compound **1.** Probability ellipsoids: 50 %. Colors: Fe (dark orange), P (pale orange), N (blue), C (gray), H (white).

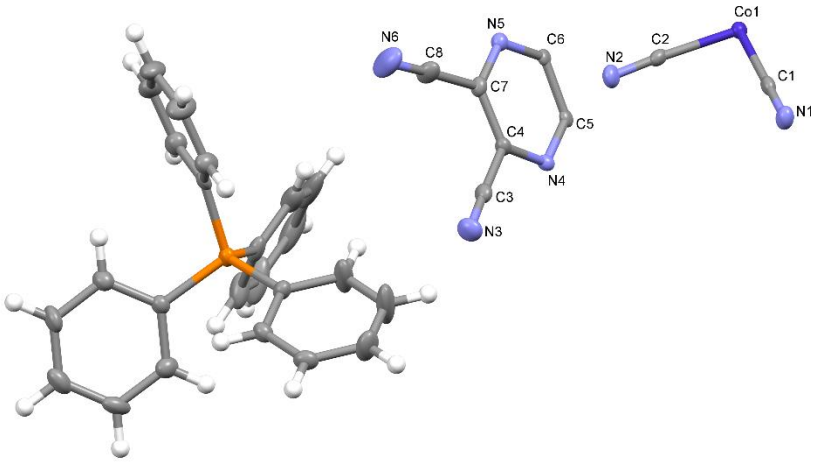

Figure S2. Asymmetric unit of compound **2.** Probability ellipsoids: 50 %. Colors: Co (dark blue), P (pale orange), N (blue), C (gray), H (white).

Table S3. Distance and angle parameters of compound **1** and **2.** (C1', C2' – means atom generated by symmetry)

Compound 1				**Compound 2**			
Parameter	**[Å]**	**Parameter**	**[deg]**	**Parameter**	**[Å]**	**Parameter**	**[deg]**
Fe1 – C1	1.953	C1 – Fe1 – C2	91.45	Co1 – C1	1.909	C1 – Co1 – C2	86.82
Fe1 – C2	1.968	C1 – Fe1 – C1'	89.30	Co1 – C2	1.921	C1 – Co1 – C1'	89.22
C1 – N1	1.147	C1 – Fe1 – C2'	86.08	C1 – N1	1.148(5)	C1 – Co1 – C2'	91.59
C2 – N2	1.156	C2 – Fe1 – C2'	93.22	C2 – N2	1.153(6)	C2 – Co1 – C2'	92.42
C3 – N3	1.136(4)	Co1 – C1 – N1	178.08	C3 – N3	1.140(6)	Co1 – C1 – N1	177.80
C4 – N4	1.453(5)	Co1 – C2 – N2	175.24	C4 – N4	1.322(4)	Co1 – C2 – N2	175.67
C5 – N4	1.339(4)			C5 – N4	1.337(6)		
C6 – N5	1.341(5)			C6 – N5	1.344(4)		
C7 – N5	1.317(3)			C7 – N5	1.318(6)		
C8 – N6	1.139(6)			C8 – N6	1.138(5)		
C3 – C4	1.453(5)			C3 – C4	1.448(7)		
C5 – C6	1.455(4)			C4 – C7	1.407(4)		
C7 – C8	1.455(6)			C5 – C6	1.410(4)		
				C7 – C8	1.455(5)		

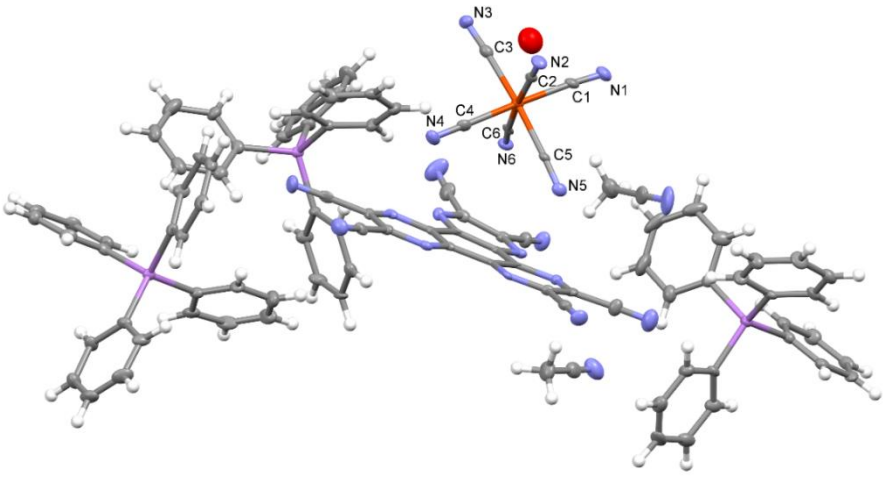

Figure S3. Asymmetric unit of compound **3.** Probability ellipsoids: 50 %. Colors: Fe (orange), As (purple), O (red), N (blue), C (gray), H (white).

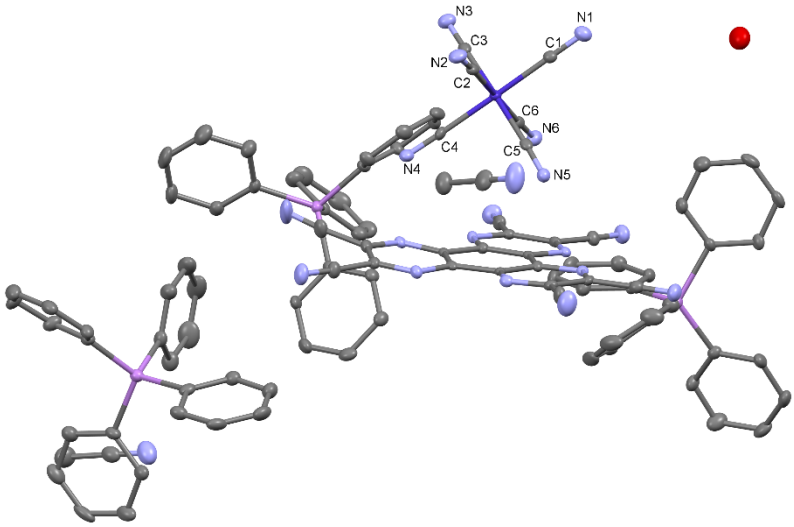

Figure S4. Asymmetric unit of compound **4.** Probability ellipsoids: 50 %. Colors: Co (dark blue), As (purple), O (red), N (blue), C (gray). Hydrogen atoms ware omitted for clarity.

Table S4. Distance and angle parameters of compound **3** and **4.**

Compound 3				Compound 4			
Parameter	**[Å]**	**Parameter**	**[deg]**	**Parameter**	**[Å]**	**Parameter**	**[deg]**
Fe1 – C1	1.972(7)	Fe1 – C1 – N1	176.1(7)	Co1 – C1	1.910(4)	Co1 – C1 – N1	179.5(4)
Fe1 – C2	1.965(6)	Fe1 – C2 – N2	179.5(6)	Co1 – C2	1.916(5)	Co1 – C2 – N2	176.0(4)
Fe1 – C3	1.967(9)	Fe1 – C3 – N3	176.3(7)	Co1 – C3	1.919(7)	Co1 – C3 – N3	176.8(5)
Fe1 – C4	1.970(8)	Fe1 – C4 – N4	178.3(7)	Co1 – C4	1.909(4)	Co1 – C4 – N4	175.4(5)
Fe1 – C5	1.952(9)	Fe1 – C5 – N5	177.5(6)	Co1 – C5	1.905(7)	Co1 – C5 – N5	177.4(5)
Fe1 – C6	1.955(6)	Fe1 – C6 – N6	175.0(6)	Co1 – C6	1.920(5)	Co1 – C6 – N6	177.7(4)
C1 – N1	1.140(10)			C1 – N1	1.150(5)		
C2 – N2	1.141(7)			C2 – N2	1.152(7)		
C3 – N3	1.150(10)			C3 – N3	1.150(8)		
C4 – N4	1.150(10)			C4 – N4	1.153(5)		
C5 – N5	1.140(10)			C5 – N5	1.153(8)		
C6 – N6	1.150(8)			C6 – N6	1.161(7)		

Additional structural views

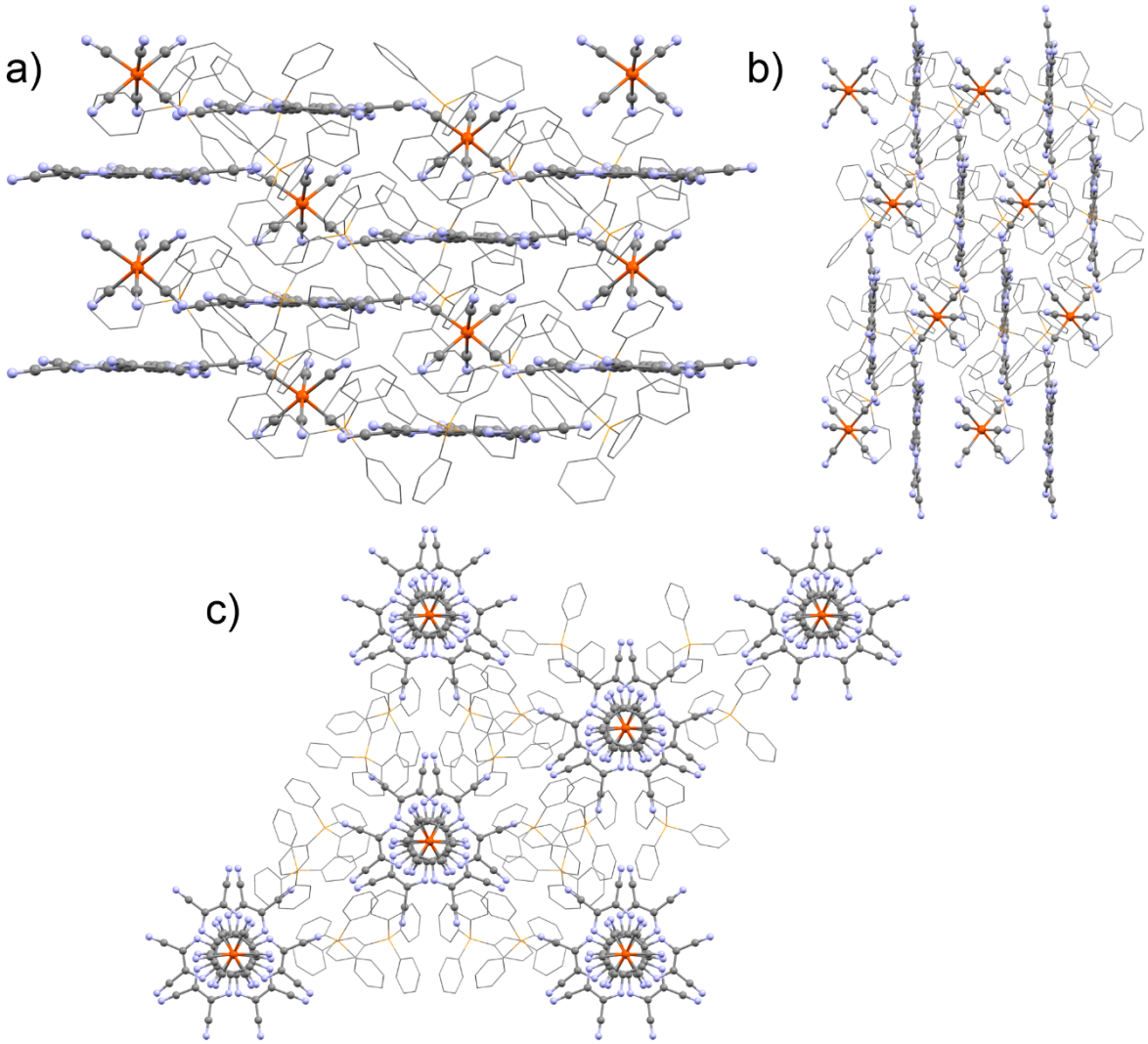

Figure S5. The crystal structure of **1** representative for compounds **1** and **2.** (a) View on crystal structure of **1** perpendicular to crystallographic a direction**.** (b) View on crystal structure of **1** perpendicular to crystallographic b direction. (c) View on crystal structure of **1** perpendicular to crystallographic c direction.

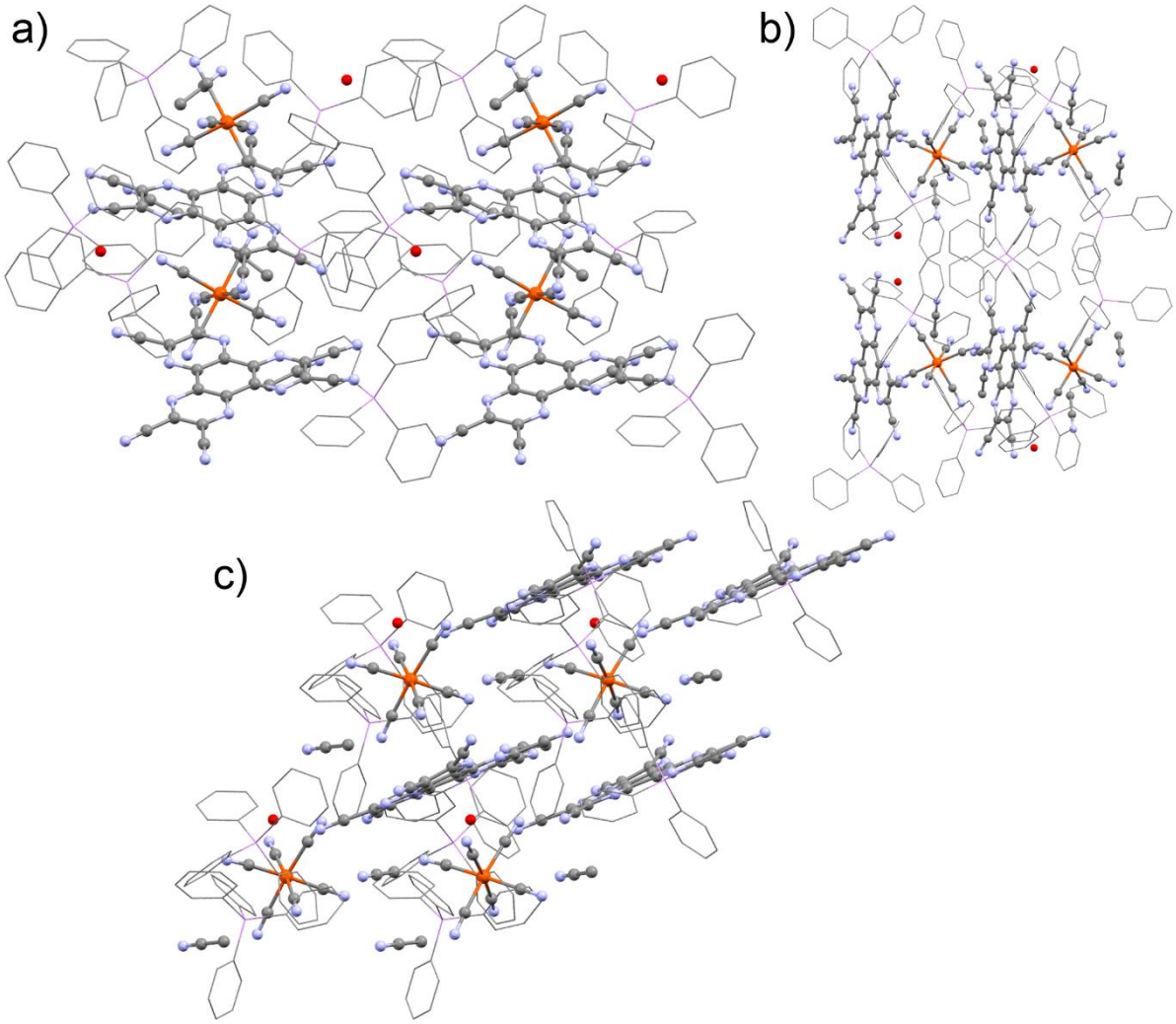

Figure S6. The crystal structure of **3** representative for compounds **3** and **4.** (a) View on crystal structure of **3** perpendicular to crystallographic a direction**.** (b) View on crystal structure of **3** perpendicular to crystallographic b direction. (c) View on crystal structure of **3** perpendicular to crystallographic c direction.

Powder X-Ray Diffraction (PXRD)

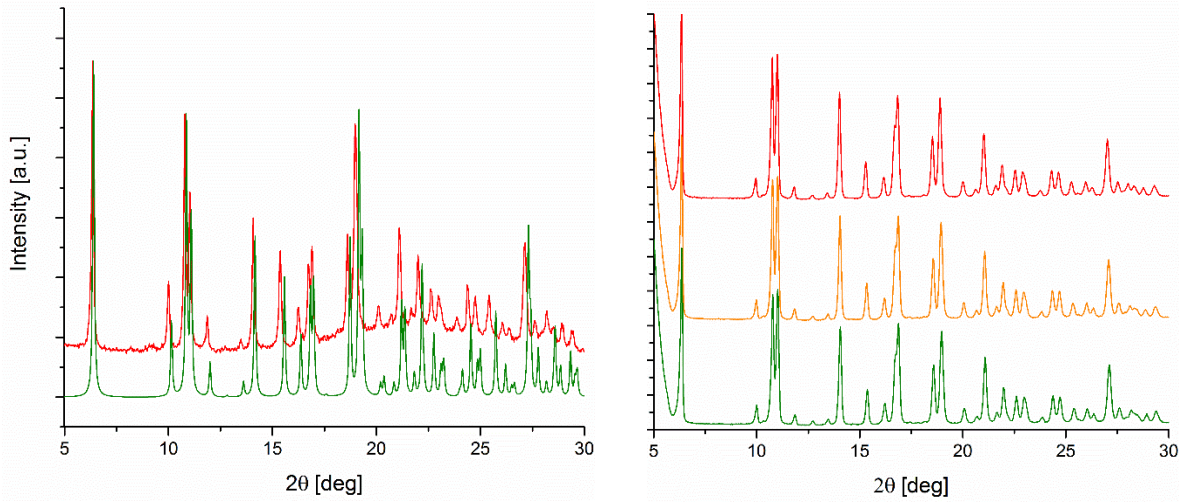

Figure S7. (Left) Powder X-ray diffraction patterns of **1** in the 5-30º range of 2Θ angle: experimental (red line) and calculated from single crystal X-ray model (green line). Shift of PXRD peaks in relation to the calculated from XRD is related to standard temperature effect. XRD (120K), PXRD (RT). (Right) The structural stability of **1** represented by the PXRD patterns in 25 ºC (green), 50 ºC (yellow) and 100 ºC (red).

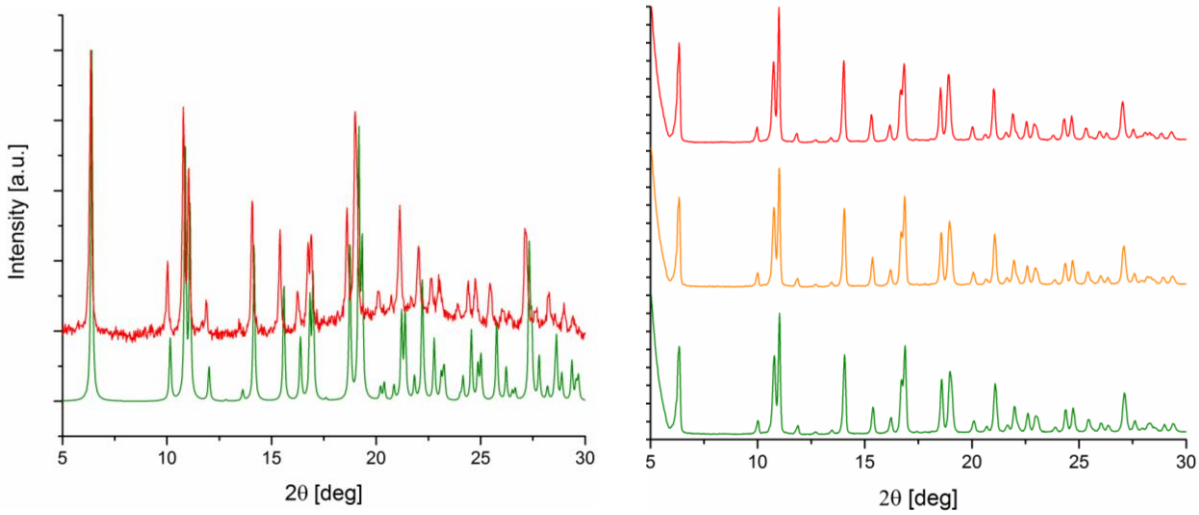

Figure S8. (Left) Powder X-ray diffraction patterns of **2** in the 5-30º range of 2Θ angle: experimental (red line) and calculated from single crystal X-ray model (green line). Shift of PXRD peaks in relation to the calculated from XRD is related to standard temperature effect. XRD (120K), PXRD (RT). (Right) The structural stability of **2** represented by the PXRD patterns in 25 ºC (green), 50 ºC (yellow) and 100 ºC (red).

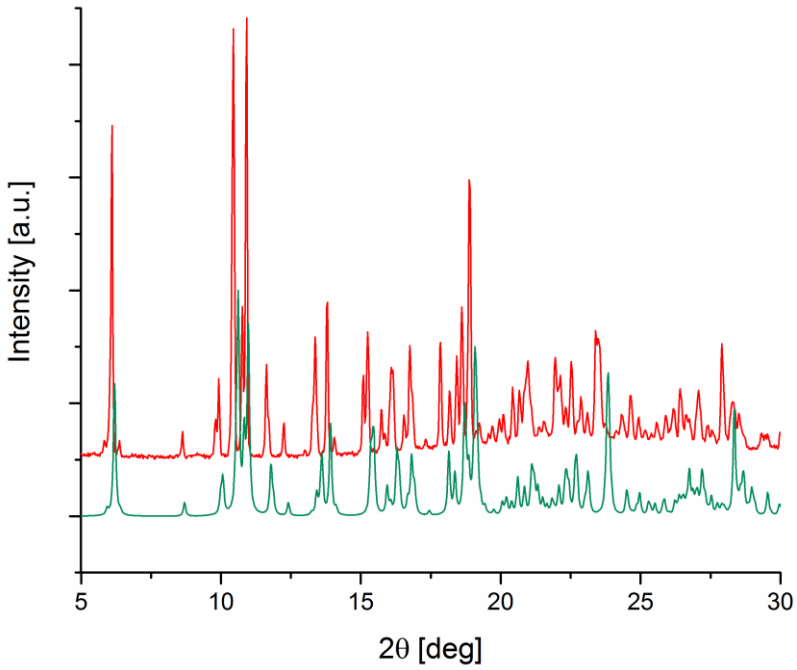

Figure S9. Powder X-ray diffraction patterns of **3** in the 5-30° range of 2Θ angle: experimental (red line) and calculated from single crystal X-ray model (green line). Shift of PXRD peaks in relation to the calculated from XRD is related to standard temperature effect. XRD (120K), PXRD (RT).

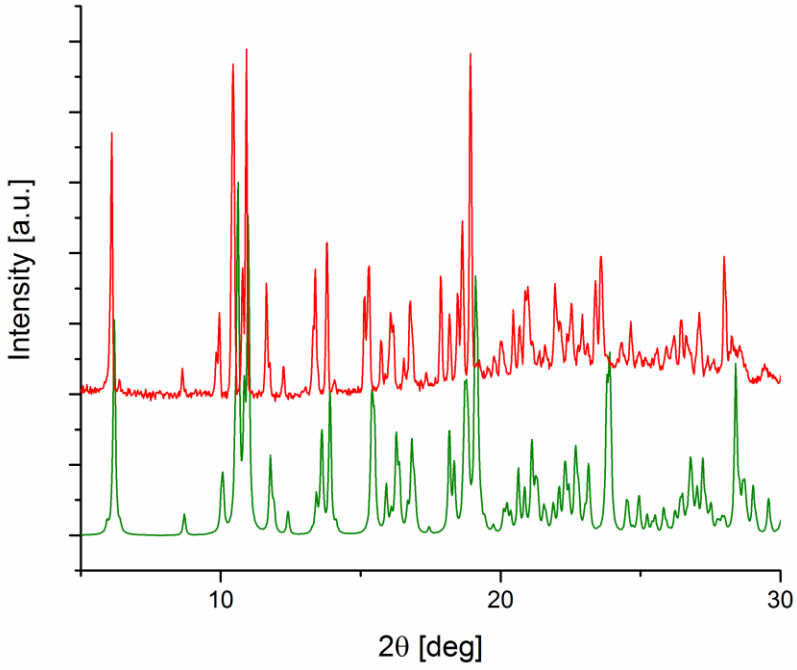

Figure S10. Powder X-ray diffraction patterns of **4** in the 5-30° range of 2Θ angle: experimental (red line) and calculated from single crystal X-ray model (green line). Shift of PXRD peaks in relation to the calculated from XRD is related to standard temperature effect. XRD (120K), PXRD (RT).

CSM Calculations

Table S5. Results of Continuous Shape Measure Analysis for $[Fe(CN)_6]^{3-}$ unit in **1**, **3** and $[Co(CN)_6]^{3-}$ unit in **2**, **4**.

Compound 1				Geometry
Centre	CSM parameters			
	OC-6	TPR-6	PPY-6	
Fe	0.165	15.043	28.682	OC-6
Compound 2				Geometry
Centre	CSM parameters			
	OC-6	TPR-6	PPY-6	
Co	0.117	15.094	28.808	OC-6
Compound 3				Geometry
Centre	CSM parameters			
	OC-6	TPR-6	PPY-6	
Fe	0.146	14.920	27.942	OC-6
Compound 4				Geometry
Centre	CSM parameters			
	OC-6	TPR-6	PPY-6	
Co	0.088	15.336	28.500	OC-6

Polyhedra codes:
OC-6 – parameter of octahedron geometry related to the Oh symmetry
TPR-6 – parameter of trigonal prism geometry related to the D3h symmetry
PPY-6 – parameter of pentagonal pyramid geometry related to C5v symmetry
CSM parameter for ideal geometry equal 0 and increase with distortion from the ideal polyhedron.

Anion-π interactions

The α_1 angle is formed between the interaction distance vector d and the vector normal to the ring plane, while the α_2 angle is formed between the vector normal to the ring plane and the vector of cyanide bond. The full set of results is presented in the Table S5.

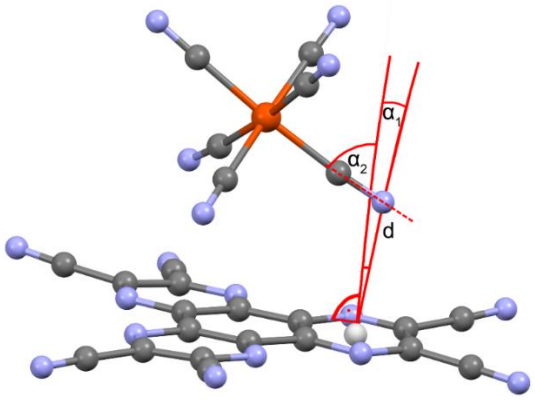

Table S6. Geometrical parameters of anion – π interactions in compounds **1-4.**

Interaction	Compound 1		Compound 2	
	α_1, α_2 (°)	d (Å)	α_1, α_2 (°)	d (Å)
$_{CN}N_1$··centr	5.1(1), 52.1(2)	2.952	2.9(1), 51.6(2)	2.945
$_{CN}N_2$··centr	6.5(1), 44,0(2)	2.990	7.1(1), 43,7(2)	2.989
Interaction	**Compound 3**		**Compound 4**	
	α_1, α_2 (°)	d (Å)	α_1, α_2 (°)	d (Å)
$_{CN}N_1$··centr	13.2(1), 42.1(2)	3.157	13.2(1), 42,6(2)	3.203
$_{CN}N_2$··centr	9.4(1), 28.3 (2)	2.934	8.5(1), 27.4 (2)	2.924
$_{CN}N_3$··centr	6.3(1), 58.0(2)	2.943	6.5(1), 56.5(2)	2.940
$_{CN}N_4$··centr	17.0(1), 38.9(2)	2.926	17.0(1), 37.9(2)	2.917
$_{CN}N_5$··centr	10.0(1), 47.8(2)	2.896	9.8(1), 47.4(2)	2.906
$_{CN}N_6$··centr	12.3(1), 30.0(2)	3.117	11.4(1), 29.9(2)	3.083

The distinguishable feature of compounds **3** and **4** is the broken symmetry along $HAT(CN)_6/M(CN)_6$ chains. The $HAT(CN)_6$ molecules in all four compounds adopt distorted geometries; they twist slightly out-of-plane in compounds **1** and **2**, for example, in response to the surrounding PPh_4^+ contacts and to the $[M(CN)_6]^{3-}$ complex above $HAT(CN)_6$, having a slightly different twist than the $[M(CN)_6]^{3-}$ complex below it. The differences in geometry above and below the approximated plane of $HAT(CN)_6$ results in two distinct data points on each plot in Figures S5b and S5c. The data points are shown above in Table S5, where α_1 = 5.1(1)°, α_2 = 52.1(2)° (**1**) and α_1 = 2.9(1)°, α_2 = 51.6(2)° (**2**) for one side of $HAT(CN)_6$

($_{CN}$N1…centr in Table S5), while on the opposite side of HAT(CN)$_6$ they are α_1 = 6.5(1)°, α_2 = 44.0(2)° (**1**) and α_1 =7.1(1)°, α_2 = 43,7(2)° (**2**) ($_{CN}$N2…centr in Table S5).

Also the distortion of HAT(CN)$_6$ is much more pronounced in the lower symmetry **3** and **4** compounds and this can be seen by the spread of data points for **3** and **4** in Fig. S5b and Fig. S5c of the main text, the data points reproduced in Table S5. This can be attributed to a severe bending of one –CN group that lies near a non-typical side interaction between this particular –CN group, the nearby CN^{-1} ligands, and a nearby crystallized H_2O molecule (Fig. S3 and Fig. S4), the latter of which is absent in **1** and **2**. The resulting anion-π interaction vector *d* is significantly longer at this contact (3.2 Å), compared to the majority of cases observed in **1**-**4**.

III. Physicochemical characterization

Thermogravimetric Analysis (TGA)

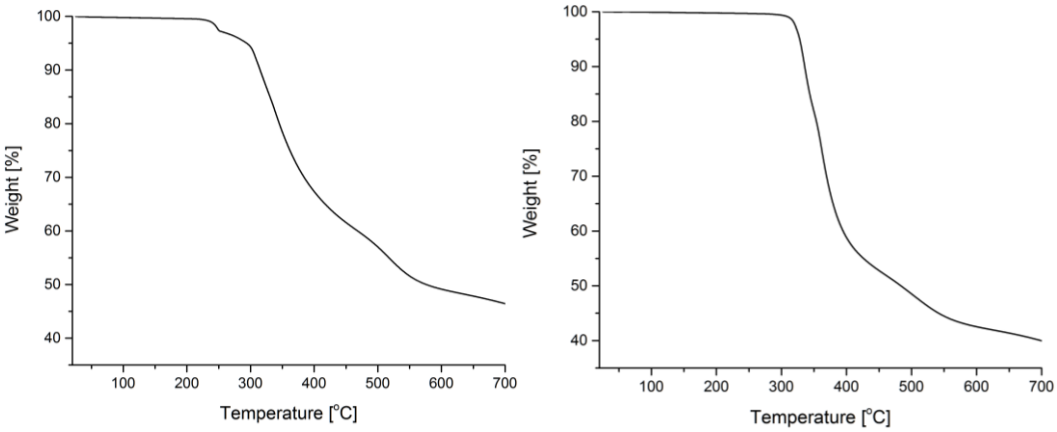

Figure S11. Thermogravimetric curves of **1** (left) and **2** (right) in 25 – 700 (^{O}C) range. No weight loss was found up to 250 ^{o}C or 300 ^{o}C, respectively.

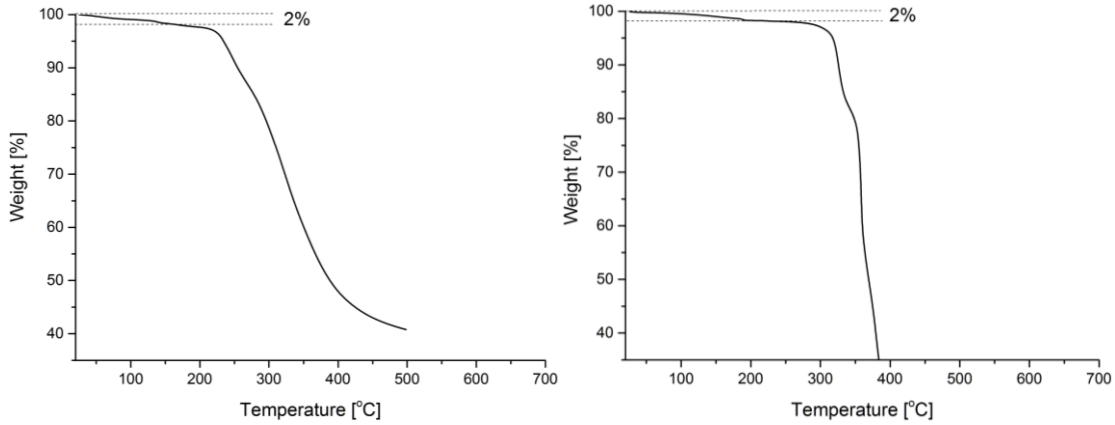

Figure S12. Thermogravimetric curves of **3des** (left) and **4des** (right). The weight loss of 2% in both cases up to 170 ^{o}C and 240 ^{o}C, respectively, corresponds to the loss of $2H_2O$ molecules per formula unit, in a perfect agreement with the results of elemental analyses (compare experimental part).

Oxidation state

(a)

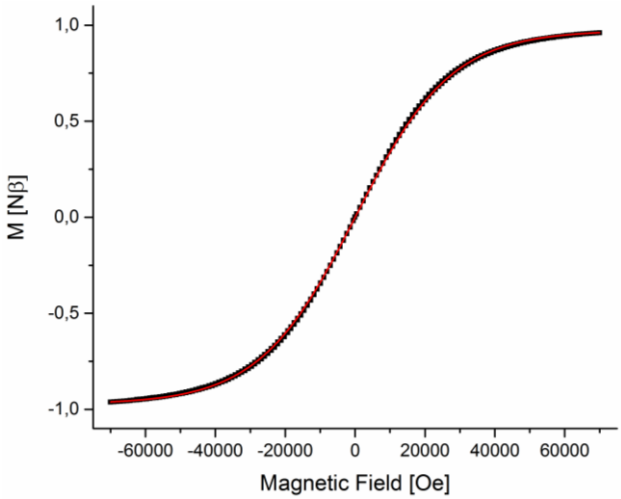

(b)

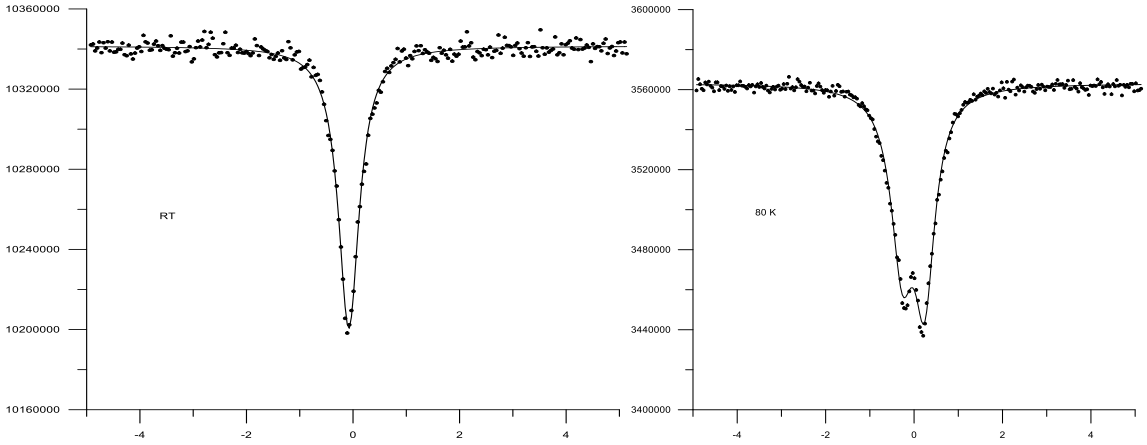

Figure S13. (a) Magnetization vs magnetic field **1** in 1.8 K: experimental (black points) and fitted using the Brillouin function assuming $S = ½$. (red line). (b) Mössbauer spectra of **1** in RT (left) and in 80 K (right). The isomeric shift close to 0 and quadrupole splitting less than 0.5 $mm \cdot s^{-1}$ are consistent with the $^{LS}Fe^{III}$ state in $[Fe(CN)_6]^{3-}$.

Table S5. Parameters of fitted Brillouin function.

Model	Brillouin Function
G	1.9460±0.0007
Magnetic Centers	1
T	1.8K
Reduced Chi-Sqr	3,85391E-5
R-Square (COD)	0.99993
Adj. R-Square	0.99993

Infrared Spectra

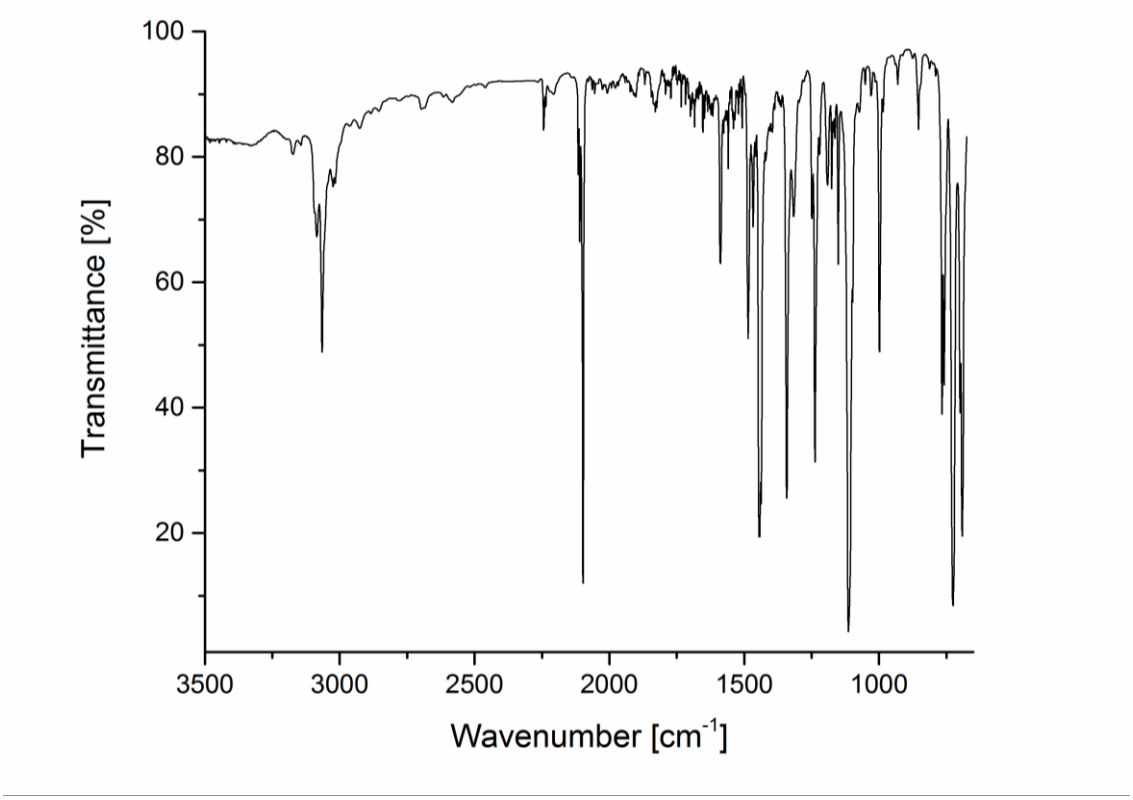

Figure S14. Infrared spectrum of **1** in 3500 – 675 cm^{-1} range.

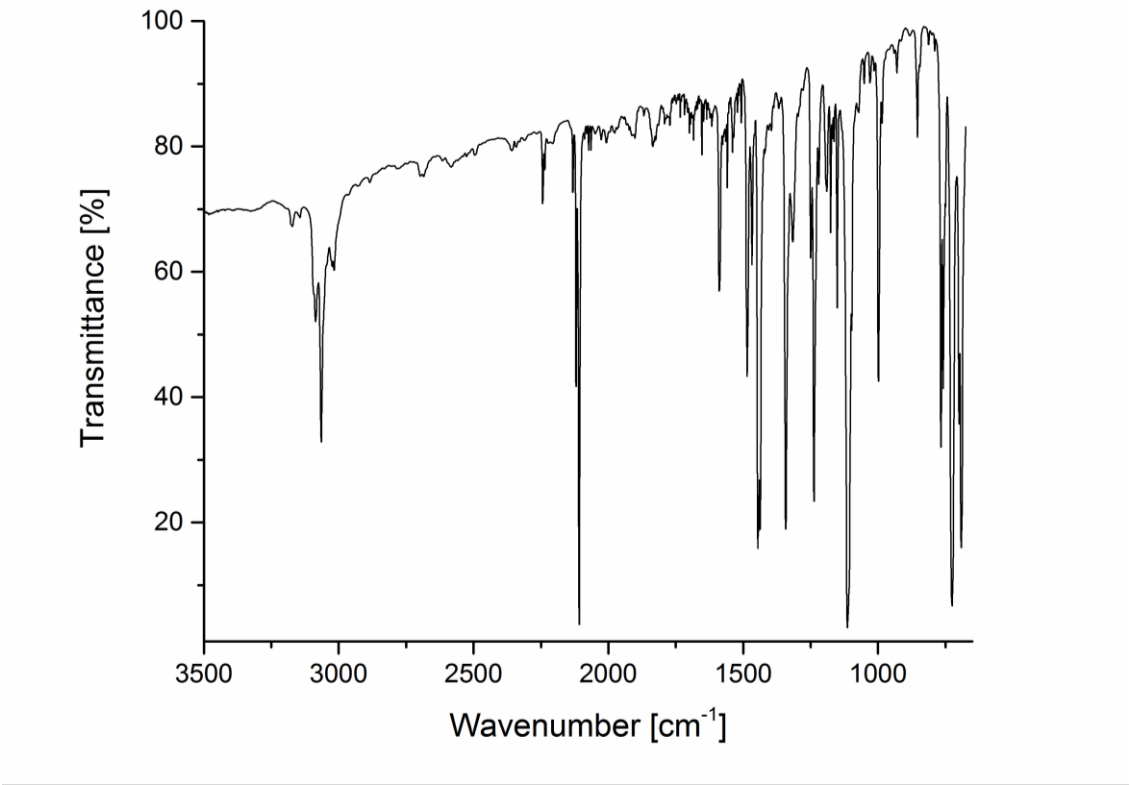

Figure S15. Infrared spectrum of **2** in 3500 – 675 cm^{-1} range.

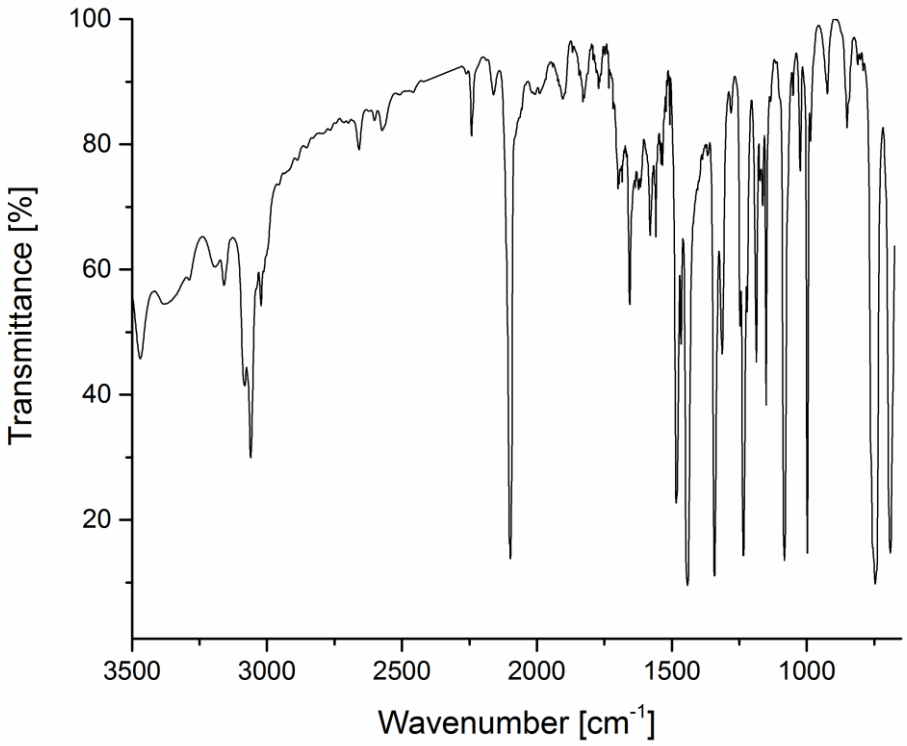

Figure S16. Infrared spectrum of **3des** in 3500 – 675 cm^{-1} range.

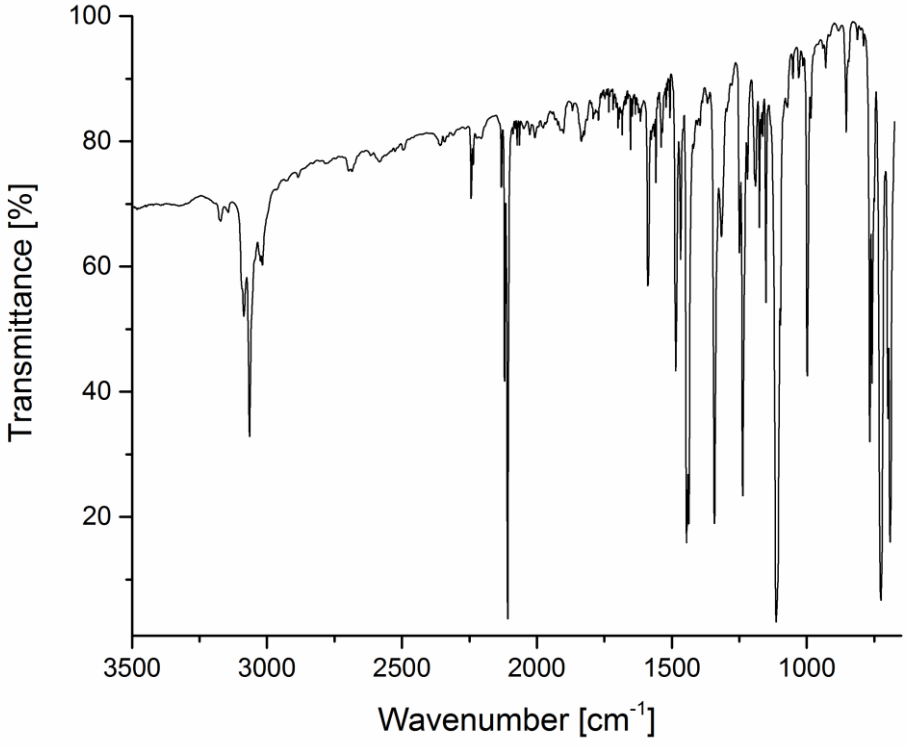

Figure S17. Infrared spectrum of **4des** in 3500 – 675 cm^{-1} range.

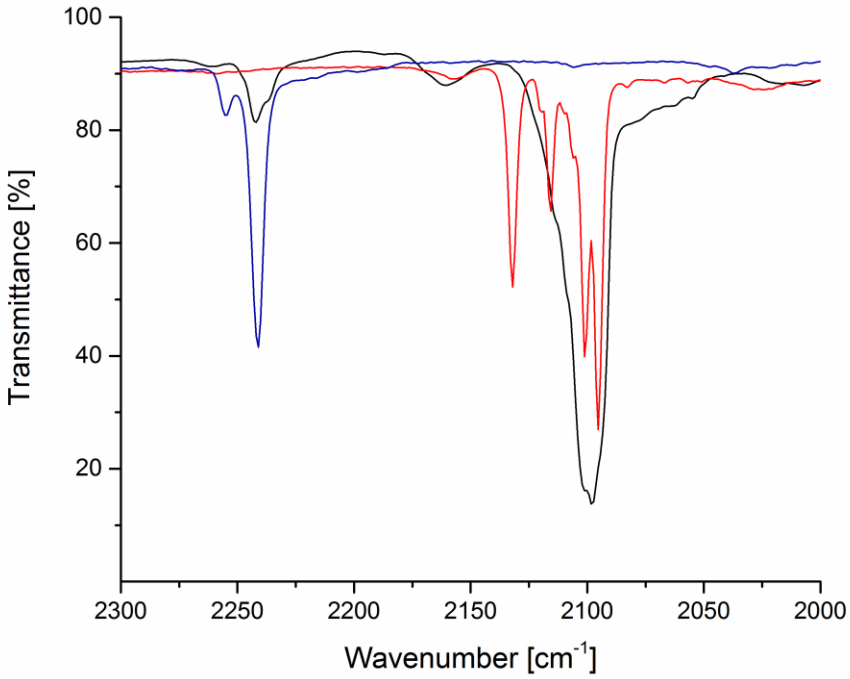

Figure S18. Compare of infrared spectrum of **3des** (black), starting complex (red) and $HAT(CN)_6$ (navy blue) in 2300 – 2000 cm^{-1} range.

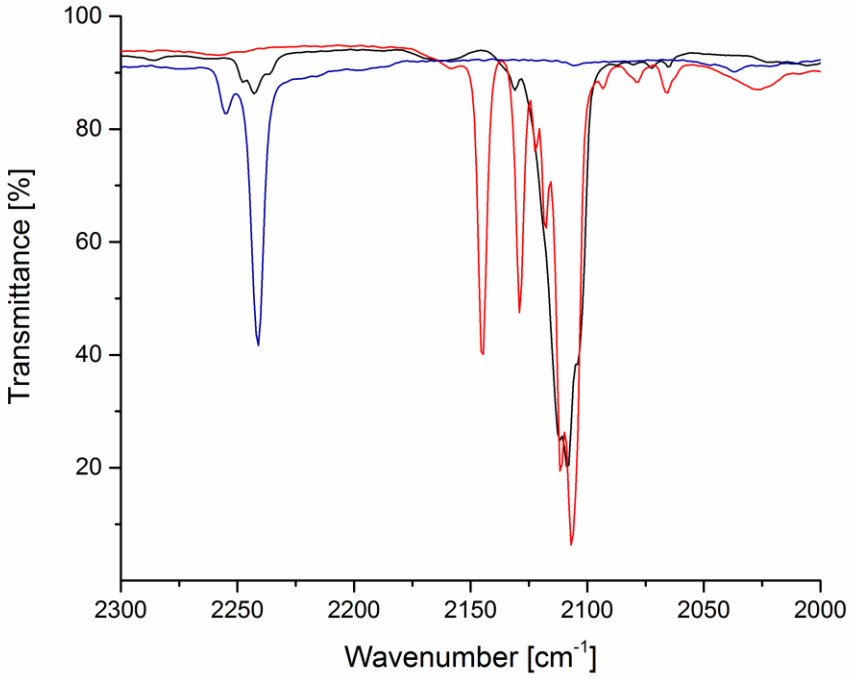

Figure S19. Compare of infrared spectrum of **4des** (black), starting complex (red) and $HAT(CN)_6$ (navy blue) in 2300 – 2000 cm^{-1} range.

UV-VIS-NIR Spectra.

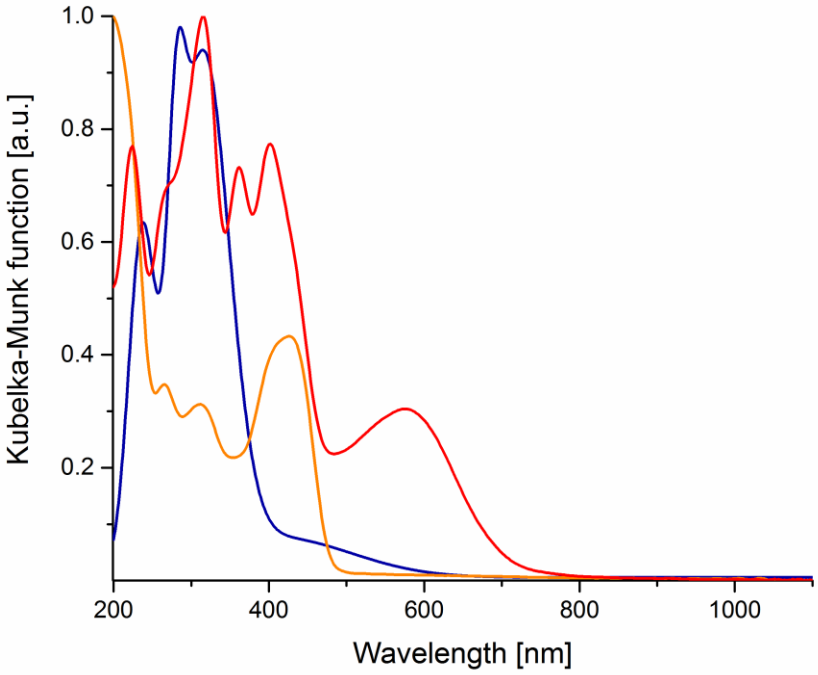

Figure S20. Compared UV-VIS-NIR solid state spectra of **3des** (red), starting complex (orange), $HAT(CN)_6$ (navy blue).

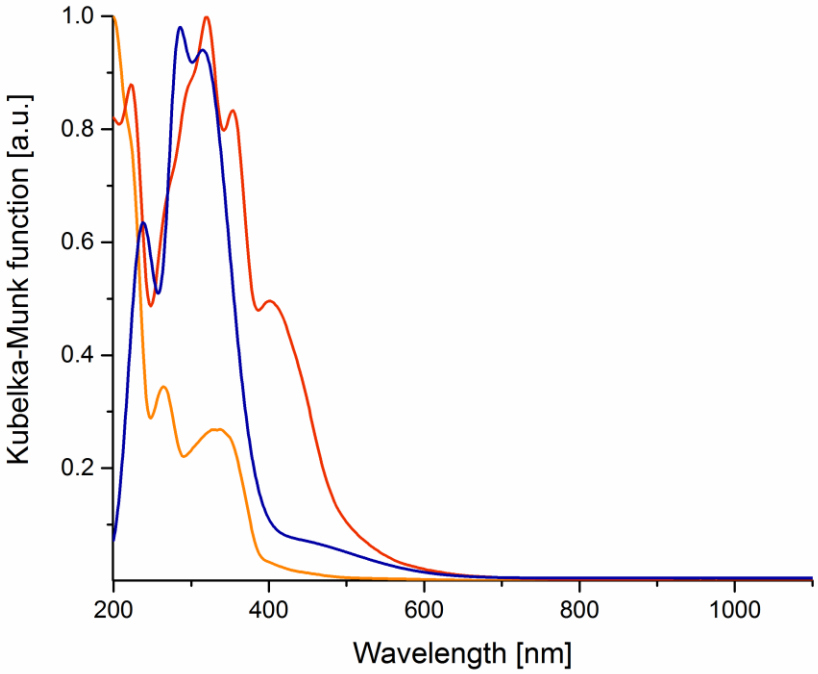

Figure S21. Compared UV-VIS-NIR solid state spectra of **4des** (red), starting complex (orange), $HAT(CN)_6$ (navy blue).

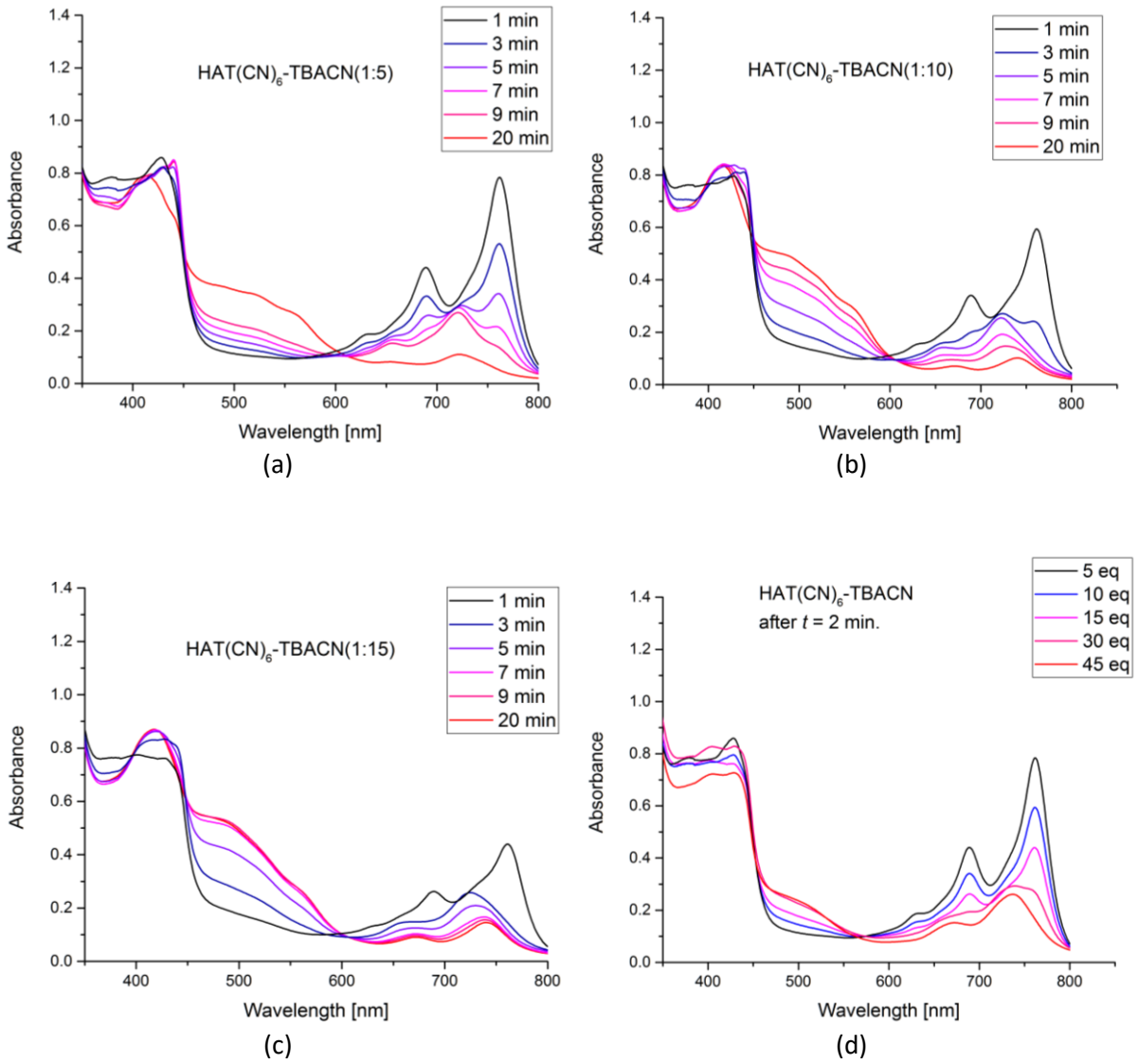

Figure S22. UV-VIS electronic spectra of $HAT(CN)_6$-TBA^+CN^- mixtures in MeCN solutions: time dependent spectra for the $HAT(CN)_6$:TBA^+CN^- molar ratio 1:5 (a), 1:10 (b) and 1:15 (c); molar ratio dependent spectra after 2 min from mixing (d).

Cyclic Voltammetry

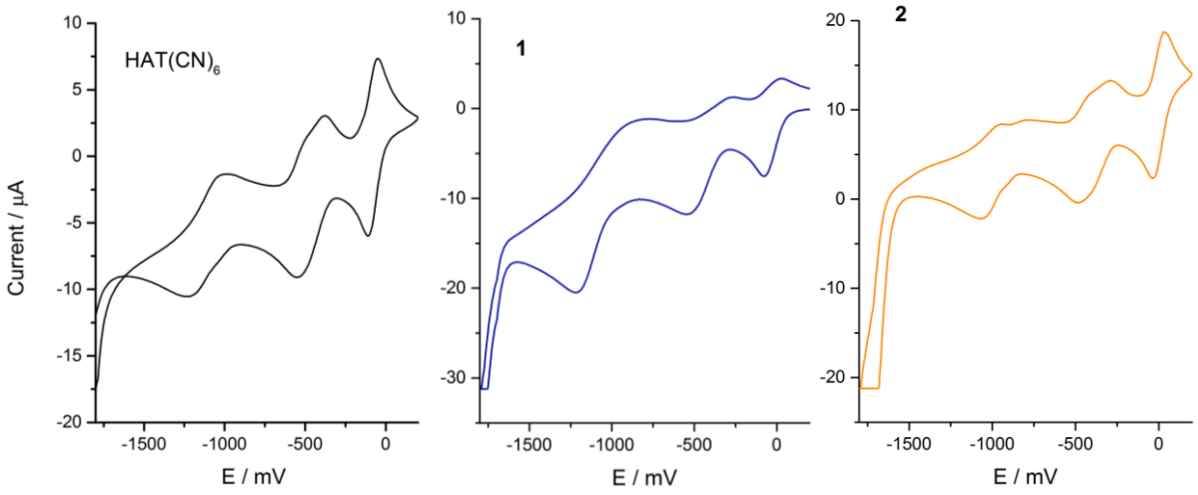

Table S8. Peaks in cyclic voltammogram of **1**, **2** and $HAT(CN)_6$

Compound	Anodic Peaks [mV]	Cathodic Peaks [mV]
$HAT(CN)_6$	-986	-1243
	-376	-551
	-51	-110
1	-776	- 1220
	-268	-548
	28	-76
2	-941	-1073
	-782	-905
	295	-485
	29	-40

IV. Computational Details and additional calculated data

Technical details of periodic models calculations: All of the reported computations used first-principles Density Functional Theory (DFT).[1] The periodic network calculations were performed with the Vienna ab-initio Simulation Package (VASP), version 5.3.5.[2] The projector augmented wave (PAW) method[3] was used to treat the core states along with a plane-wave basis set with an energy cutoff of either 400 eV, for geometry optimizations, or 500 eV, for computing electronic charge densities and electrostatic potential (ESP) maps. The H 1s, C, N 2s/2p, P, Si 3s/3p, As, Ge 4s/4p, and Fe, Co 4s/3d electrons were treated explicitly in the calculations. We used the GGA functional of Perdew-Burke-Ernzerhof (PBE)[4] in tandem with the 3rd-generation Grimme set of semiempirical dispersion corrections[5] (PBE-D3), as implemented when using the IVDW=12 tag that is available in VASP.[6] The k–point grids were generated using the Γ–centered Monkhorst–Pack scheme, and the number of divisions along each reciprocal lattice vector was chosen such that the product of this number with the real lattice constant was 10 Å in the geometry optimizations, and 30 Å otherwise. The geometries of all the structures were converged such that the magnitude of the largest force acting on the constituent atoms was less than, at most, 0.02 eV/Å^2. The atomic coordinates of all of the crystal structures were optimized using the cell parameters that were obtained from X-ray diffraction studies. Additionally, a Hubbard correction potential was used, within the framework of the GGA+U method[7] without LSDA exchange splitting. The calculations presented in this report used U-J=2. U-J=0 and U-J=4 were also used in order to compute ΔE_{int} for compounds **2** and **4** and toensure that the results were qualitatively similar; it was found that the interaction energy of $HAT(CN)_6$ was unaffected by U-J ranging from 0 to 4, but the band gap, as could be expected, was found to increase with larger values of U-J. The qualitative features and differences of the DOS plots were described similarly for all the U-J values, particularly: 1) the $HAT(CN)_6$ character of the conduction bands, 2) the $M[(CN)_6]^{3-}$ character of the valence bands, and 3) the influence of the spin density near the Fermi energy in compound **1**. We also computed the electronic structures of compounds 1 and 2, in their PBE+D3+2U geometries, with the HSE06 functional[8] in order to compare their band gaps when they are independent on the U-J parameter. The Bader charges were computed by using a freely available script[9] to parse the topology of the computed valence charge density.

*Definition of ΔE_{int}(**X**) for periodic models*: The interaction energy of $HAT(CN)_6$ in compound **X**, ΔE_{int}(**X**), was computed as:

$$\Delta E_{int}(\mathbf{X}) = E_{\mathbf{X}} - (E_{\mathbf{X}\text{-HAT}} + E_{HAT}),$$

where $E_{\mathbf{X}}$ is the DFT electronic ground-state energy of compound **X**, $E_{\mathbf{X}\text{-HAT}}$ is the energy of compound **X** with the $HAT(CN)_6$ molecules removed, and E_{HAT} is the energy of the $HAT(CN)_6$ sublattice when frozen in the geometry that it assume in compound **X**. As such, ΔE_{int}(**X**) includes the interactions of $HAT(CN)_6$ with everything else in the crystal, not just with the $[M(CN)_6]^{3-}$ complexes.

Analogously, the charge density difference in compound **X**, CDD(**X**) can be defined as:

$$CDD(\mathbf{X}) = \Delta\rho(\mathbf{X}) = \rho_{\mathbf{X}} - (\rho_{\mathbf{X}\text{-HAT}} + \rho_{HAT})$$

where ρ_X is the computed electronic charge density of **X**.

To estimate the strength of the $[M(CN)_6]^{3-}$-$HAT(CN)_6$ interactions in compound **X**, we computed a corrected interaction energy, $\Delta E_{int,\ HAT/MCN}$(**X**), as

$$\Delta E_{int,\ HAT/MCN}(\mathbf{X}) = \Delta E_{int}(\mathbf{X}) - (E_{\mathbf{X}\text{-MCN},15\rightarrow14} - E_{\mathbf{X}\text{-MCN-HAT},15\rightarrow14} - E_{HAT})$$

where $E_{\mathbf{X}\text{-MCN},15\rightarrow14}$ is the DFT electronic ground-state energy of compound **X** with the $[M(CN)_6]^{3-}$ complexes removed and the P/As atoms replaced with Si/Ge, $E_{\mathbf{X}\text{-MCN-HAT},15\rightarrow14}$ is the electronic energy of compound **X** with the $[M(CN)_6]^{3-}$ and $HAT(CN)_6$ complexes removed and the P/As atoms replaced with Si/Ge, and E_{HAT} is the electronic energy of the $HAT(CN)_6$ sublattice when frozen in the geometry that they assume in compound **X**. The substitution of P/As with Si/Ge is necessary to balance the charge in the periodic simulation cell and is, itself, an approximation. We have estimated the impact that such a substitution has on the binding energies with a non-periodic molecular cluster of $HAT(CN)_6$ and $APh_4^{\{0,+\}}$ molecules (where A = Si/Ge for APh_4, or P/As for APh_4^+); this is illustrated below in Fig. S26 where, overall, the substitution was found to have a small effect on the binding energy of $HAT(CN)_6$ in the molecular cluster.

A comment on the treatment of dispersion forces: We note that the post-SCF dispersion correction that was used in our PBE-D3 models accounts, in itself, for 60% of the total interaction energies. Since the inclusion of dispersion effects is so important in these systems, we also computed the interaction energy for compounds **1**, **2** and **4** with another type of DFT functional that accounts for dispersion forces in a modified Hamiltonian, the vdW-optB88 type of functional.[10] We found the vdW-optB88 functional to predict larger (more negative) interaction energies: $\Delta E_{int,optB88}$(**1**) = -158, $\Delta E_{int,optB88}$ (**2**) = -161, and $\Delta E_{int,optB88}$ (**4**) = -161 kcal·mol^{-1}. These represent an increase of 25-30% vs. the PBE-D3 interaction energies, further illustrating how important the inclusion/treatment of dispersion effects is to these systems. Our estimate of the interaction energy between $HAT(CN)_6$ and $[M(CN)_6]^{3-}$ in compound **2** was found to be $\Delta E_{int,\ HAT/MCN}$(**2**) = -93 kcal·mol^{-1} with vdW-optB88, a 15% increase over the PBE-D3 estimate. This suggests that we are likely underestimating the strength of the interaction energies in the main text. The computed band structures and density of states plots with the vdW-optB88 functional were found to agree very well the PBE-D3 functional. In this respect, we are confident that the treatment of dispersion with a post-SCF dispersion correction is sufficient here, within the framework of DFT, in emphasizing the importance of the $HAT(CN)_6$-$[M(CN)_6]^{3-}$ interactions to the total interaction energy.

Technical details of molecular cluster (non-periodic) models calculations: Dispersion-corrected DFT-D3[5] calculations, using the Amsterdam Density Functional (ADF) package, version 2013.01,[11] were also performed on selected molecular clusters extracted directly from the optimized coordinates of **1** and **2**. The computations employed the PBE functional[4] and a relativistic all-electron triple-ξ doubly polarized (TZ2P) basis set from the ADF basis set library. Scalar relativistic effects were incorporated in the computations by means of the Zeroth-Order Regular Approximation (ZORA).[12] Interaction between fragments was analyzed by means of the Extended Transition State – Natural Orbitals for Chemical Valence (ETS-NOCV) charge and energy decomposition scheme.[13]

Extended Transition State – Natural Orbitals for Chemical Valence (ETS-NOCV) method: In the original Extended transition state (ETS) method, the interaction energy, ΔE_{int}, between the fragments in the geometry of the system is divided into following components:

$$\Delta E_{int} = \Delta E_{elstat} + \Delta E_{Pauli} + \Delta E_{orb} (+ \Delta E_{disp})$$

The first term, ΔE_{elstat}, corresponds to the classical electrostatic interaction between the fragments in the combined system. The second component, ΔE_{Pauli}, accounts for the repulsive Pauli interaction between occupied orbitals on the two fragments. The third term, ΔE_{orb}, represents the stabilizing interactions between the occupied molecular orbitals on one fragment with the unoccupied molecular orbitals of the other fragment (corresponding to inter-fragments donation and back-donation charge transfers), as well as the mixing of occupied and virtual orbitals within the same fragment (intra-fragment polarization, charge redistribution). The last contribution, ΔE_{disp}, obtained at DFT-D3 level,

referred to as the dispersion term, corresponds to the dispersion interaction between the fragments in the combined system.

The natural orbitals for chemical valence (NOCV) are eigenvectors that diagonalize the charge density difference matrix. The NOCV pairs (ψ_{-k} , ψ_k) decompose the charge density difference CDD into NOCV contributions, $CDD_{NOCV\,k}$:

$$CDD = \sum_{k=1}^{M/2} v_k \left[-\psi_{-k}^2 + \psi_k^2 \right] = \sum_{k=1}^{M/2} CDD_{NOCV\,k}$$

where v_k / M stand for the NOCV eigenvalues / the number of basis functions. Visual inspection of $CDD_{NOCV\,k}$ plots helps to attribute symmetry and the direction of the charge flow. Within the ETS-NOCV scheme, information gained from the analysis of $CDD_{NOCV\,k}$ plots can be enriched by providing the orbital energy contributions $\Delta E_{NOCV\,k}$ from $CDD_{NOCV\,k}$ to the total orbital interaction energy ΔE_{orb}.

Additional calculated data:

Electrostatic Potential (ESP) Maps and Charge Density Difference (CDD) Plots

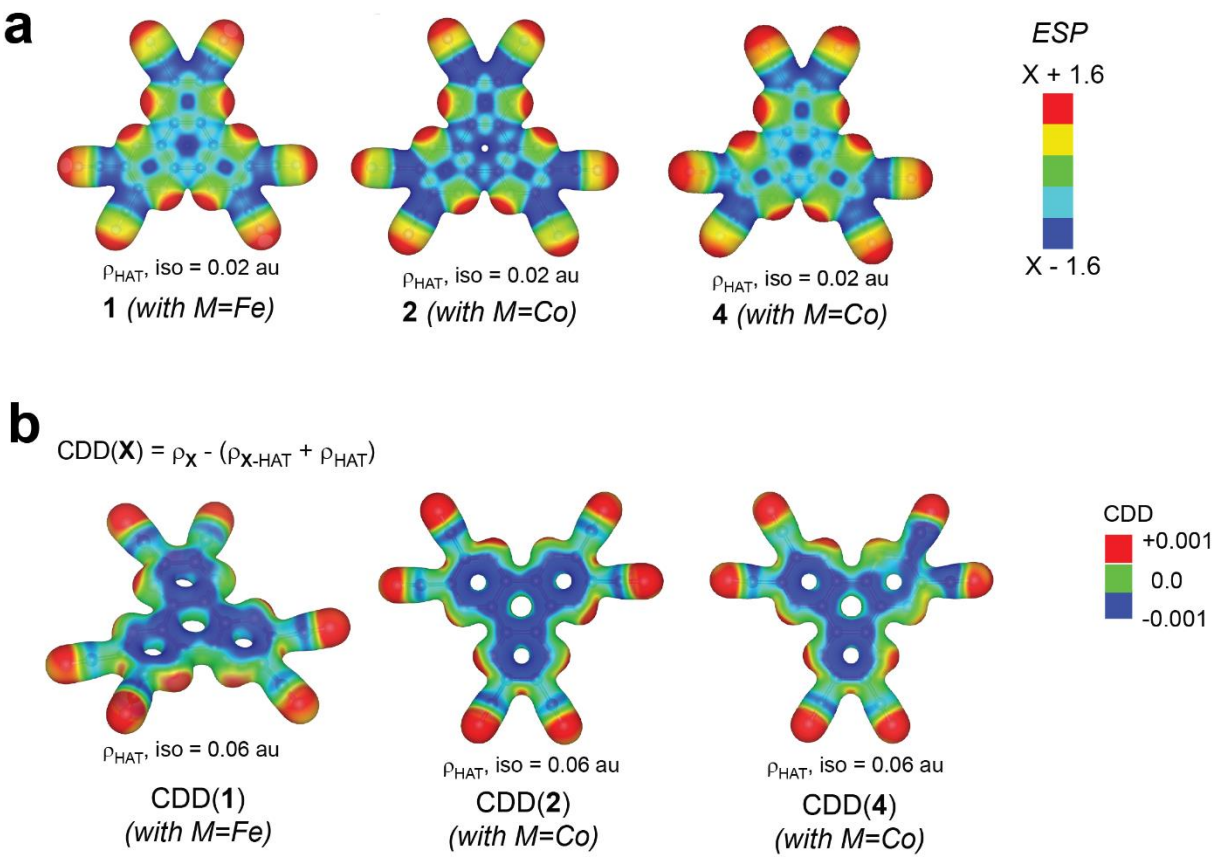

Figure S23. (a) The computed electrostatic potential (ESP) around $HAT(CN)_6$ in three crystal structures: (left) in compound **1**, (middle) in compound **2**, and (right) in compound **4**. The ESP is coloring an isosurface of the total electron density from a single $HAT(CN)_6$ molecule. (b) The charge density difference (CDD) surrounding a $HAT(CN)_6$ in (left) compound **1**, (middle) compound **2**, and (right) compound **4**. The CDD is coloring an isosurface of the total electron density from a single $HAT(CN)_6$ molecule.

Figure S23 shows the computed ESP and CDD profiles, as shown for **2** in Figure 3 of the main text, for compounds **1**, **2**, and **4**. They can all be seen to be quite similar in these representations, but a broken

symmetry in the CDD around $HAT(CN)_6$ is visible in compound **4**; this broken symmetry comes about from the asymmetrically crystallized H_2O molecule.

Computed Band Structures and Densities of States

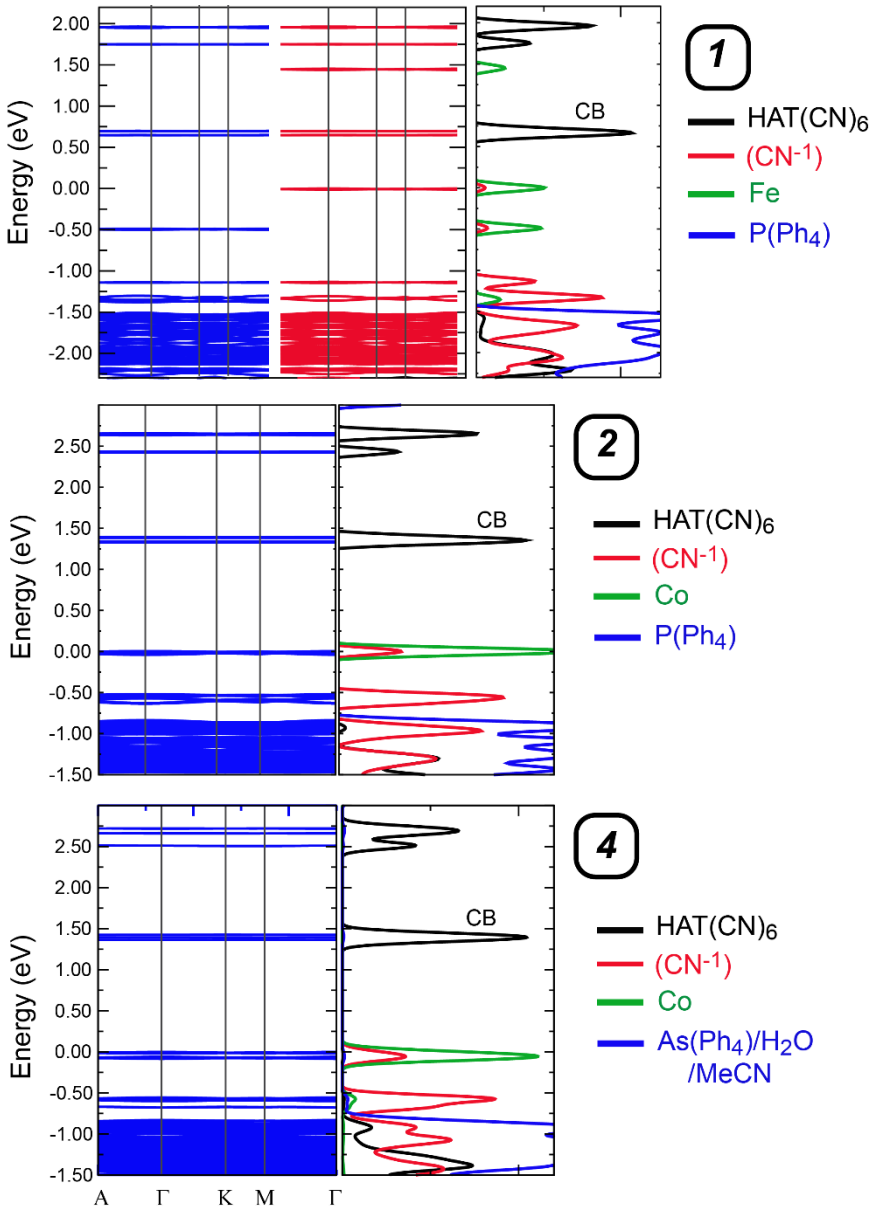

Figure S24. The computed (PBE-D3+U; U-J=2 eV) electronic band structures of compounds **1** (top), **2** (middle), and **4** (bottom). The two spin components are shown for compound **1** as blue and red; compounds **2** and **4** have closed-shell electronic configurations. The Fermi energy is set to zero in each plot. Summed atom-projected density of states, the PDOS - computed electronic density of states projected onto the atoms of the molecular building blocks, are shown to the right of each band structure. The PDOS was computed with electronic smearing (SIGMA=0.06 eV in VASP) to help with its visibility. The lines in the PDOS are colored according to the building block to which they correspond, and the location of the conduction band, "CB", is shown.

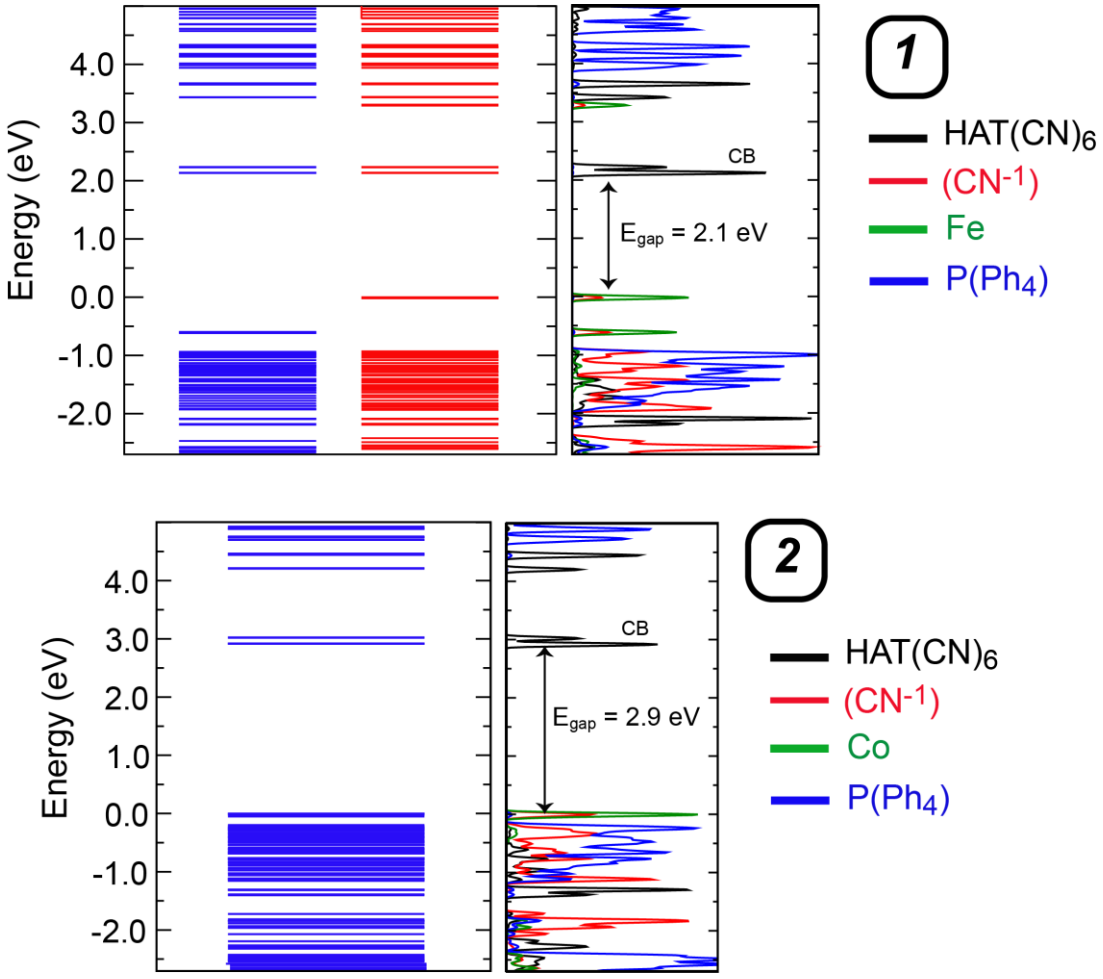

Figure S25. The computed electronic band energies of compounds **1** (top), and **2** (bottom) when computed with a single k-point with the hybrid HSE06 density functional. The two spin components are shown for compound **1** as blue and red; compound **2** has a closed-shell electronic configuration. The Fermi energy is set to zero in each plot. Summed atom-projected density of states, ie. the PDOS – the computed electronic density of states projected onto the atoms of the molecular building blocks, are shown to the right of each band structure. The PDOS was computed with electronic smearing (SIGMA=0.02 eV in VASP) to help with its visibility. The lines in the PDOS are colored according to the building block to which they correspond, and the location of the conduction band, "CB", is shown.

With both the PBE+D3+U (Figure 24) and HSE06 (Figure S25) functionals, the conduction bands in every compound were found to have π-symmetry $HAT(CN)_6$ character. The occupied bands near the Fermi energy have $M[(CN)_6]^{3-}$ character. We note that there are conceptual differences which relate with the presence/absence of spin density near the band gap in **1**/**2**, most obviously the smaller band gap in **1** *vs* **2** and the Fe-based band that lies over 3.0 eV above the Fermi energy in **1**. This suggests tangible electronic structure differences between **1** and **2** that would influence their electronic excitations.

Estimating the interactions between $HAT(CN)_6$ and APh_4

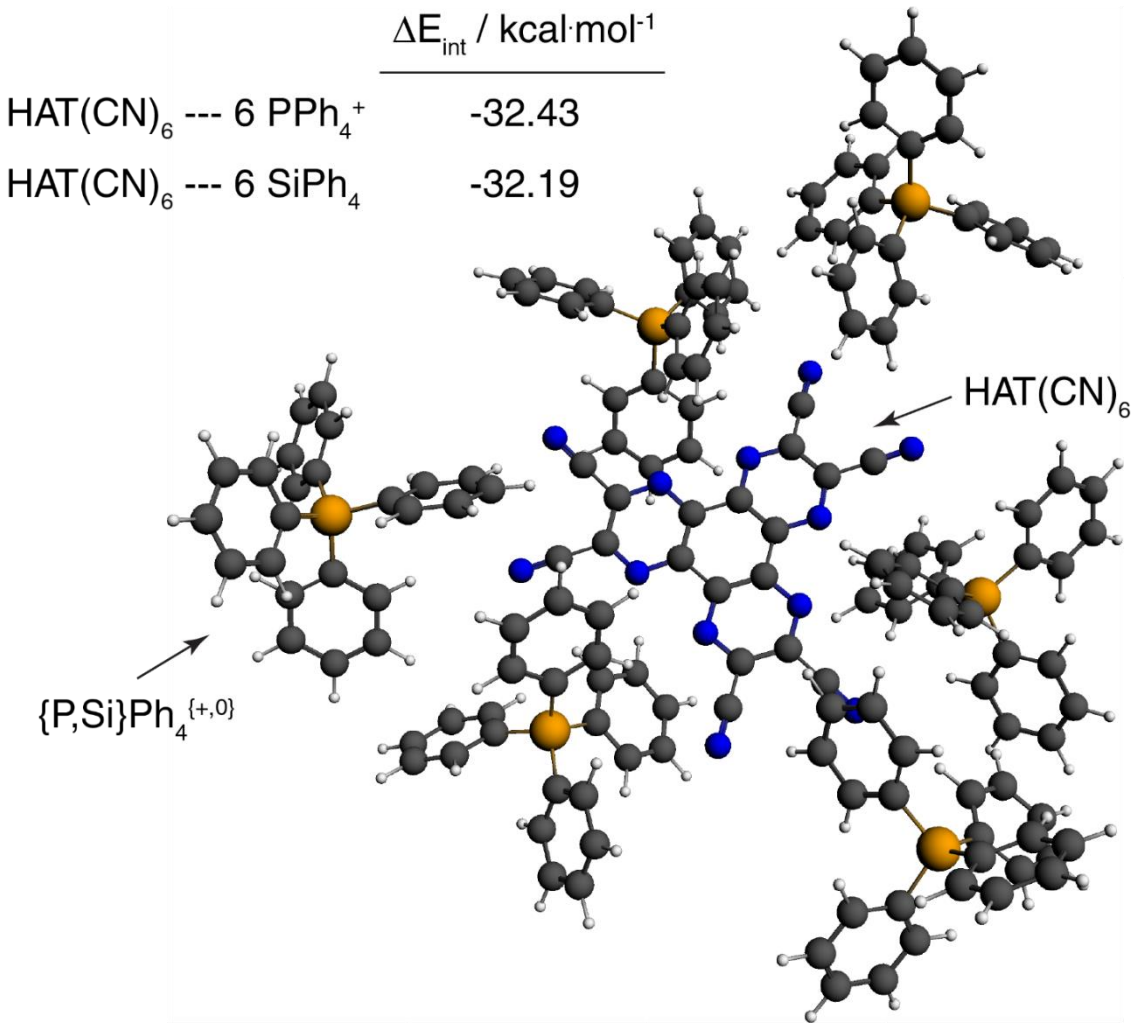

Figure S26. Interaction energy between $HAT(CN)_6$ and a XPh_4^n network (X = P, n = +1; X = Si, n = 0) in a molecular cluster extracted from the optimized geometry of compound **2**.

The molecular cluster that was extracted from compound **2** to study the interaction of $HAT(CN)_6$ with the $\{P,Si\}Ph_4^{\{+,0\}}$ network is shown in Figure S26; it consists of one $HAT(CN)_6$ molecule surrounded by six PPh_4^+ / $SiPh_4$ molecules. The substitution of P with Si is found to have a small effect on the binding energy when frozen the network in the geometry that was obtained in compound **2**.

ETS-NOCV Analysis

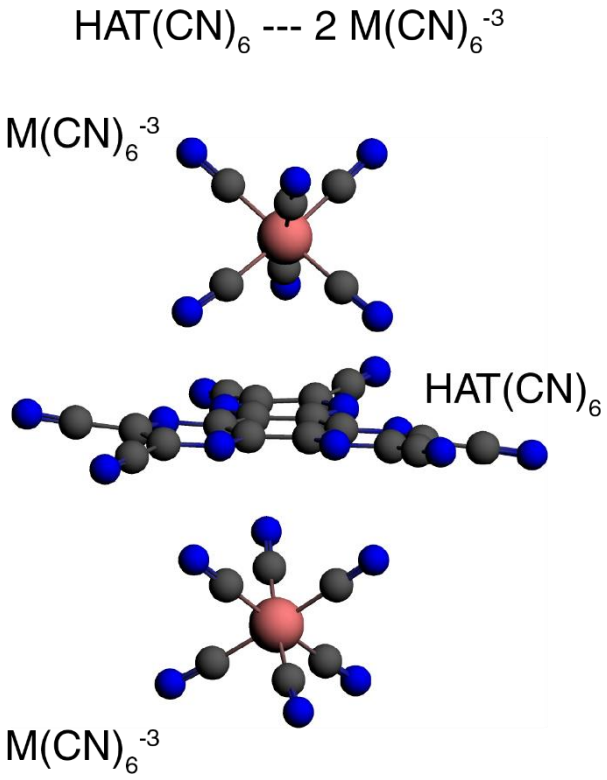

	M = Fe^{III}	Co^{III}
ΔE_{int}	-150.53	-150.92
ΔE_{orb}	-	-56.70
ΔE_{Pauli}	-	34.24
ΔE_{elstat}	-	-112.19
ΔE_{disp}	-	-16.26

Figure S27. Structure of the molecular clusters that were extracted from compounds **1** and **2**. The interaction energy and its decomposition (in kcal·mol^{-1}) within the ETS scheme are shown in the table below.

The total interaction energy of $HAT(CN)_6$ in the molecular cluster geometries that are extracted from **1** and **2** are comparable with each other, like they are in the periodic calculations, but both are substantially higher than the -78 to -81 kcal/mol estimates that were obtained from the periodic calculations. This is not unexpected considering the large contribution of the electrostatic term, ΔE_{elstat}, to the total interaction energy. Since the charge deformation density of the molecular cluster resembles the charge deformation density of the periodic crystal, we focus here on ΔE_{orb}, the contribution that comes about from charge transfer between and within fragments.

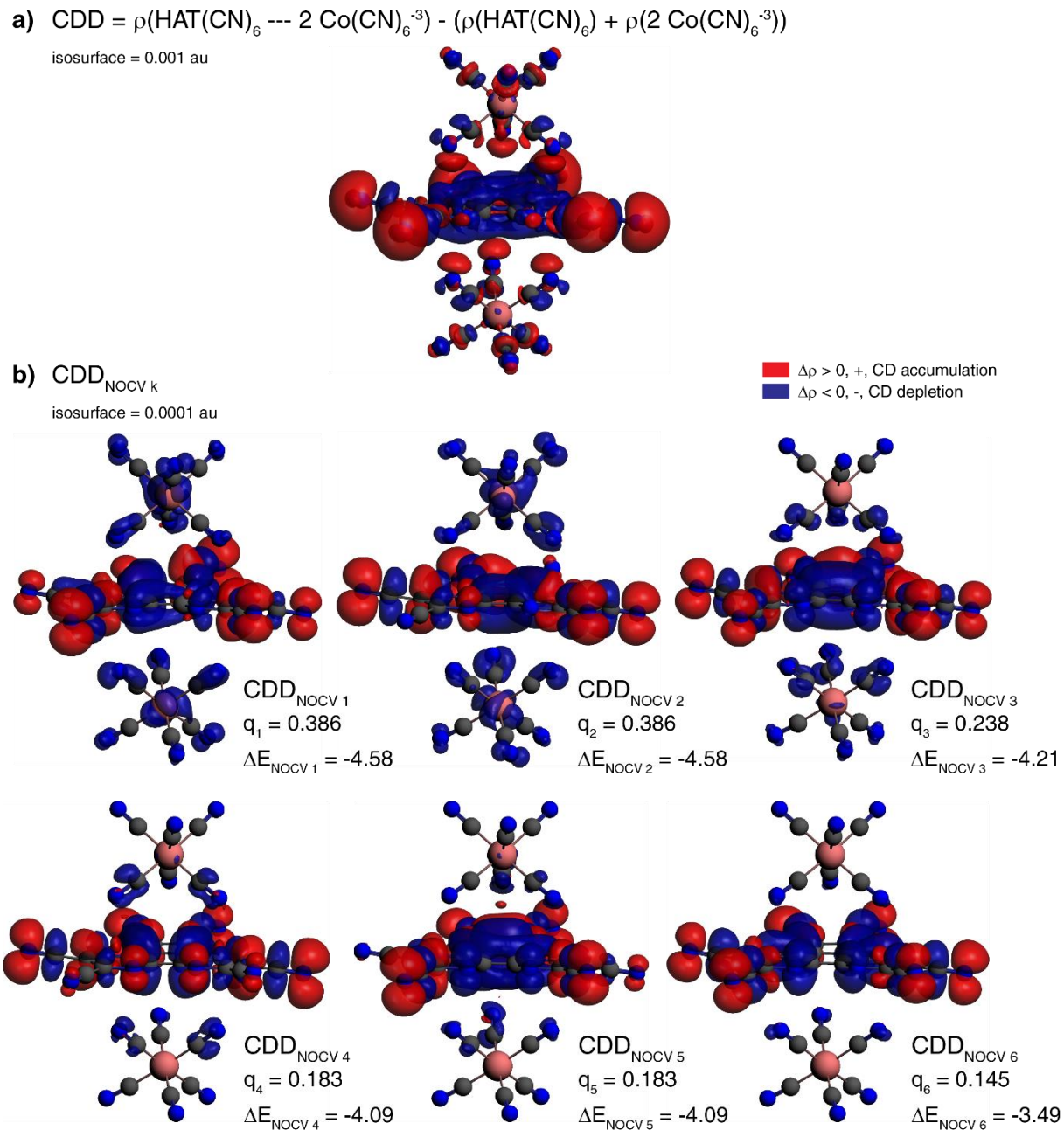

Figure S28. (a) The total charge deformation density (CDD) of the molecular cluster extracted from compound **2** (it is identical to the CDD that is shown in Figure 3c of the main text). (b) The six largest contributions to the CDD that arise from an ETS-NOCV analysis of the molecular cluster. Isosurfaces of the charge deformation densities that are associated with each NOCV contribution, $CDD_{NOCV\ k}$, are shown. Also shown alongside each $CDD_{NOCV\ k}$ is its corresponding charge transfer ($q_k = v_k$) and its contribution to the orbital interaction energy (ΔE_{NOCV} k in kcal·mol^{-1}). Red / blue indicates a gain-of-charge / loss-of-charge, respectively.

V. References

[1] W. Kohn, L. J. Sham, *Phys. Rev.* 1965, **140**, A1133.

[2] (a) G. Kresse, J. Hafner, *Phys. Rev. B* 1993, **47**, 558; (b) G. Kresse, J. Furthmuller, *Phys. Rev B*. 1996, ***54***, 11169.

[3] (a) P. E. Blöchl, *Phys. Rev. B* 1994, **50**, 17953; (b) G. Kresse, D. Joubert, *Phys. Rev. B* 1999, **59**, 1758.

[4] (a) J. P. Perdew, K. Burke, M. Ernzerhof, *Phys. Rev. Lett.* 1996, ***77***, 3865; (b) J. P. Perdew, K. Burke, M. Ernzerhof, *Phys*. *Rev*. *Lett*. 1997, **78**, 1396.

[5] S. Grimme, J. Antony, S. Ehrlich, H. Krieg, *J. Chem*. *Phys*. 2010, **132**, 154104.

[6] S. Grimme, S. Ehrlich, L. Goerigk, *J. Comp. Chem*. 2011, **32**, 1456.

[7] A. I. Liechtenstein, V. I. Anisimova, J. Zaanen, *Phys. Rev. B*. 1995, **52**, R5467.

[8] A. V. Krukau , O. A. Vydrov, A. F. Izmaylov, and G. E. Scuseria, *J. Chem. Phys.* 2006, **125**, 224106.

[9] W. Tang, E. Sanville, G. Henkelman, *J. Phys.: Condens. Mat.* 2009, **21**, 084204.

[10] (a) J. Klimes, D. R. Bowler, A. Michaelides, *J. Phys.: Condens. Mat.* 2010, **132**, 022201; (b) M. Dion, H. Rydberg, E. Schroder, D. C. Langreth, B. I. Lundqvist, *Phys. Rev. Lett*. 2004, **92**, 246401.

[11] (*a*) ADF2013, SCM, Theoretical Chemistry, Vrije Universiteit, Amsterdam, The Netherlands, http://www.scm.com; (*b*) C. F. Guerra, J. G. Snijders, G. te Velde, E. J. Baerends, *Theor. Chem. Acc.* 1998, **99**, 391; (*c*) G. te Velde, F. M. Bickelhaupt, E. J. Baerends, C. F. Guerra, S. J. A. van Gisbergen, J. G. Snijders, T. Ziegler, *J. Comput. Chem.* 2001, **22**, 931.

[12] (*a*) E. van Lenthe, E. J. Baerends, J. G. Snijders, *J. Chem*. *Phys*. 1993, **99**, 4597; (*b*) E. van Lenthe, E. J. Baerends, J. G. Snijders, *J. Chem*. *Phys*. 1994, **101**, 9783; (*c*) E. van Lenthe, A. E. Ehlers, E. J. Baerends, *J. Chem*. *Phys*. 1999, **110**, 8943; *d*) E. van Lenthe, J. G. Snijders, E. J. Baerends, *J. Chem*. *Phys*. 1996, **105**, 6505.

[13] (*a*) M. Mitoraj, A. Michalak, *J. Mol. Model.* 2007, **13**, 347; *(b*) M. P. Mitoraj, A. Michalak, T. Ziegler, *J. Chem*. *Theory Comput*. 2009, **5**, 962.